RESEARCH ARTICLE

Expression of IMPACT Curtails Metabolic Plasticity and Augments NK Cell Killing to Abrogate Metastatic Growth

Surajit Sinha[1], Abir Kumar Panda[2], Rodrigo Xavier das Neves[3], Zeribe C. Nwosu[4], Ke Xu[5], Elke van Beek[6], Priyanka P. Desai[1], Sivasish Sindiri[7], Sruthi Chempati[2], Kirsten Remmert[1], Billel Gasmi[7], Linda Bojmar[8], Constantinos Zambirinis[8], Alexander J. Rossi[9,10], Reed I. Ayabe[11], Michael M. Wach[12], James D. McDonald[13], Samantha M. Ruff[14], Emily A. Verbus[15], Areeba Saif[16], Alyssa V. Eade[1], Carolina M. Larrain[1], Lindsay R. Friedman[1], Shreya Gupta[17], Alok Ranjan[18], Martha E. Teke[19], Tahsin M. Khan[20], Tracey Pu[1], Amber Leila Sarvestani[21], Carrie E. Ryan[22], Jacob T. Lambdin[23], Kenneth Luberice[24], Stephanie N. Gregory[25], Stephanie C. Lux[26], Hanna Hong[27], Allen J. Luna[28], Imani A. Alexander[29], Sarfraz R. Akmal[25], Shahyan U. Rehman[30], Ashley Rainey[1], Todd D. Prickett[6], Vishal N. Koparde[31,32], Samantha Sevilla[31,32], Skyler A. Kuhn[33], King Chan[34,35], Zhonghe Sun[35], Nina Bubunenko[35], Eileen Li[36], Cathleen Hannah[1], Geneti Gaga[37], Thorkell Andresson[34,35], Margaret C. Cam[31,32], Xiaolin Wu[35], Lisa M. Jenkins[38], Andrew M. Blakely[1], Jeremy L. Davis[39], Giorgio Trinchieri[3], Pankaj K. Singh[40], James C. Yang[5], Marina Pasca di Magliano[41,42], Costas A. Lyssiotis[4,42,43], Michael B. Yaffe[44], Ethan M. Shevach[2], and Jonathan M. Hernandez[1,45]

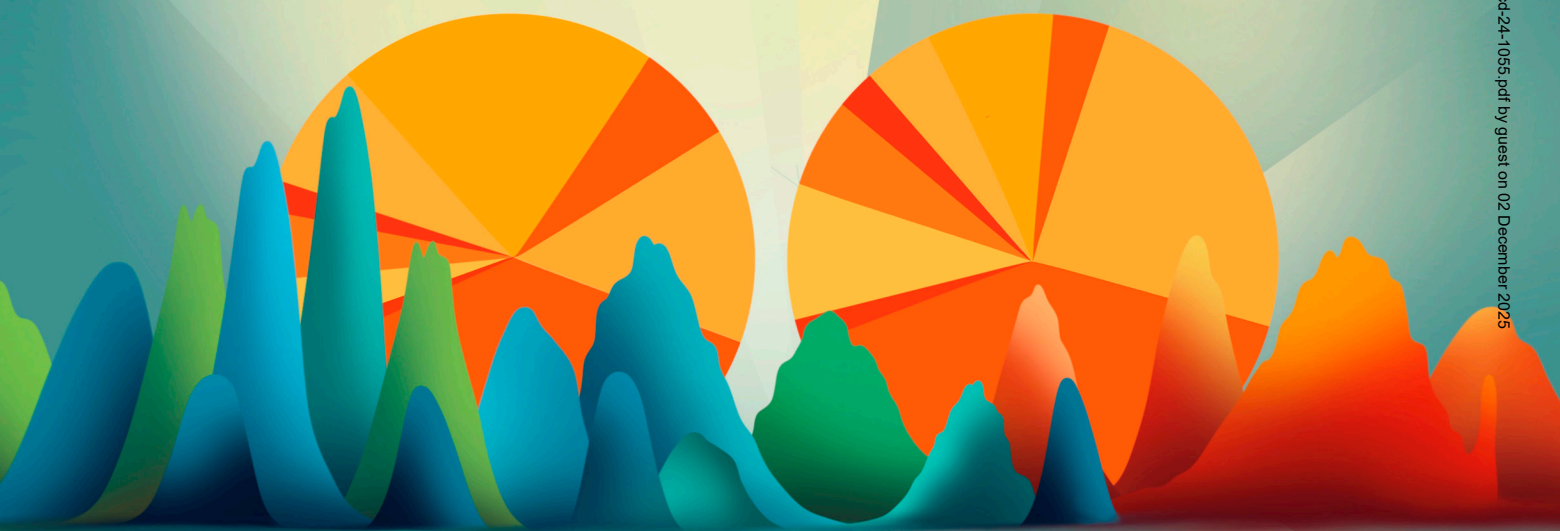

ABSTRACT Given the propensity of aggressive epithelial tumors to form hepatic metastases, we performed an *in vivo* cDNA screen using the mouse liver and *KRAS*^{G12D}/*TP53*^{R273H} pancreatic cells that identified the RNA-binding protein GCN1 as an integral component of hepatic outgrowth. RNAi experiments reveal that GCN1 triggers the integrated stress response (ISR) to activate serine, folate, and methionine biosynthetic pathways together with amino acid transporters, which act in concert to facilitate acquisition of metabolites and to restore redox homeostasis. Alongside the activation of the ISR, we found that GCN1 also functions in the nucleus where it interacts with HNRNPK to suppress the expression of MHC-I molecules and NK ligands. Intriguingly, we identified IMPACT as an endogenous competitive inhibitor of GCN1 that blocks both ISR-dependent metabolic control and disrupts HNRNPK interaction. In doing so, IMPACT enhances tumor immunogenicity to unleash NK cell killing, in addition to sensitizing metastatic tumor cells to immune checkpoint blockade.

SIGNIFICANCE: Metastatic tumor cells display profound immunometabolic plasticity to colonize distant organs. We identify IMPACT, an inhibitor of GCN1-stress signaling, expression of which curtailed metabolic plasticity and augmented tumor immunogenicity, sensitizing metastatic tumor cells to NK cell–mediated destruction.

[1]Surgical Oncology Program, NCI, National Institutes of Health, Bethesda, Maryland. [2]Cellular Immunology Section, NIAID, National Institutes of Health, Bethesda, Maryland. [3]Laboratory of Integrative Cancer Immunology, National Institutes of Health, Bethesda, Maryland. [4]Department of Molecular and Integrative Physiology, University of Michigan, Ann Arbor, Michigan. [5]Department of Surgery, Brigham and Women's Hospital, Boston, Massachusetts. [6]University Medical Center Utrecht, Utrecht, the Netherlands. [7]Surgery Branch, National Cancer Institute, National Institutes of Health, Bethesda, Maryland. [8]Department of Biomedical and Clinical Sciences, Linkoping University, Linkoping, Sweden. [9]Department of Colon and Rectal Surgery, Oschner Health, New Orleans, Louisiana. [10]Department of Surgery, Oschner Health, New Orleans, Louisiana. [11]Division of Hepatobiliary and Pancreas Surgery, Department of Surgery, Complex General Surgical Oncology, University of California, Irvine, Orange, California. [12]Department of Surgical Oncology, University of Pittsburgh Medical Center, Pittsburgh, Pennsylvania. [13]Complex General Surgical Oncology, University Surgical Oncology, University of Tennessee, Knoxville, Tennessee. [14]Department of Surgical Oncology, Complex General Surgical Oncology, Emily Couric Clinical Cancer Center, University of Virginia, Charlottesville, Virginia. [15]Department of Surgery, Cleveland Clinic, Cleveland, Ohio. [16]Department of Surgery, UT Health McGovern Medical School, Houston, Texas. [17]Department of Surgery, Colorectal Surgery, Cleveland Clinic, Warrensville Heights, Ohio. [18]Department of Pharmacology and Toxicology, Massey Cancer Center, Richmond, Virginia. [19]Department of Surgery, UT Southwestern Medical Center, Dallas, Texas. [20]Department of Surgical Oncology, Complex General Surgical Oncology, University of Pittsburgh Medical Center, Pittsburgh, Pennsylvania. [21]Department of Surgery, University of Missouri Kansas City, Kansas City, Missouri. [22]Department of Surgery, University of Buffalo, Buffalo, New York. [23]Department of Surgery, George Washington University, Washington, District of Columbia. [24]Department of Surgery, University of Florida Health – Jacksonville, Jacksonville, Florida. [25]Department of Surgery, Robert Wood Johnson Medical School, Rutgers University, New Brunswick, New Jersey. [26]Northwestern Feinberg School of Medicine, Chicago, Illinois. [27]Cleveland Clinic Lerner College of Medicine, Cleveland, Ohio. [28]School of Medicine, Vanderbilt University, Nashville, Tennessee. [29]Rutgers New Jersey Medical School, Newark, New Jersey. [30]Department of Surgery, Yale School of Medicine, New Haven, Connecticut. [31]Collaborative Bioinformatics Resource, Center for Cancer Research, National Cancer Institute, National Institutes of Health, Bethesda, Maryland. [32]Advanced Biomedical Computational Sciences, Frederick National Laboratory for Cancer Research, Leidos Biomedical Research, Inc., Frederick, Maryland. [33]Integrated Data Sciences Section, Research Technology Branch, NIAID, National Institutes of Health, Bethesda, Maryland. [34]Protein Characterization Group, Cancer Research Technology Program, Frederick National Laboratory for Cancer Research, Leidos Biomedical Research, Inc., Frederick, Maryland. [35]Cancer Research Technology Program, Frederick National Laboratory for Cancer Research, Leidos Biomedical Research, Inc., Frederick, Maryland. [36]University of Pittsburgh, Pittsburgh, Pennsylvania. [37]Laboratory Animal Sciences Program, NCI, National Institutes of Health, Bethesda, Maryland. [38]Mass Spectrometry Resource, Laboratory of Cell Biology, CCR, NCI, National Institutes of Health, Bethesda, Maryland. [39]Division of Surgical Oncology, Department of Surgery, University of Maryland Medical System, Baltimore, Maryland. [40]College of Medicine, The University of Oklahoma, Oklahoma City, Oklahoma. [41]Rogel Cancer Center, University of Michigan, Ann Arbor, Michigan. [42]Department of Surgery, University of Michigan, Ann Arbor, Michigan. [43]Division of Gastroenterology, Department of Internal Medicine, University of Michigan, Ann Arbor, Michigan. [44]MIT Center for Precision Cancer Medicine, Koch Institute for Integrative Cancer Research, Cambridge, Massachusetts. [45]Center for Immuno-Oncology, National Cancer Institute, National Institutes of Health, Bethesda, Maryland.

Corresponding Authors: Surajit Sinha, National Cancer Institute, National Institutes of Health, 10 Center Drive, Room: 3W-5840, Bethesda, MD 20892. E-mail: surajit.sinha@nih.gov; and Jonathan M. Hernandez, National Cancer Institute, National Institutes of Health, 10 Center Drive, Room: 4W-3752, Bethesda, MD 20892. E-mail: jonathan.hernandez@nih.gov

Cancer Discov 2025;15:2344–73

doi: 10.1158/2159-8290.CD-24-1055

INTRODUCTION

The metastatic cascade is a complicated series of steps that, when successfully executed, results in the appearance of radiographically apparent disease at site(s) remote from the primary tumor (1). Despite the knowledge that metastases are responsible for the overwhelming majority of cancer deaths, prevention has proved exceedingly difficult. Cancer genomic studies have identified few recurrent metastasis-specific mutations, indicating that determinants of successful outgrowth are likely related to modifiable gene expression (2). Accordingly, metastasis-initiating cells have demonstrated remarkable plasticity through the utilization of many genes, allowing successful circumvention of microenvironment-specific hurdles (3–5). For patients with gastrointestinal cancers, liver metastases are very common, frequently result in morbidity, and limit overall survival (OS). For example, nearly half of patients with localized pancreatic cancer who undergo curative-intent surgery will develop recurrence of disease in the liver following primary tumor extirpation (6).

From a tumor cell–intrinsic perspective, the liver microenvironment differs substantially from that of the primary tumor and presents significant challenges for the newly arriving tumor cell(s). For example, the liver maintains energy balance through the biosynthesis and breakdown of glucose, fatty acids, ketones, and protein, but this requires high oxygen tension markedly different from poorly vascularized pancreas tumors (7). The liver also has a robust NK cell repertoire to neutralize threats arising from exposure to dietary and microbial products from the gut (8). We recently characterized the molecular, cellular, and metabolic profiles of intraoperatively collected liver biopsies among patients with localized pancreatic adenocarcinoma (PAAD) undergoing resection (9). In doing so, we identified and defined metabolic alterations in the livers of patients with primary pancreatic cancer that differed significantly from the livers of patients without pancreatic cancer (e.g., arginine metabolism and urea cycle), including a panel of 15 metabolites that associated with subsequent liver metastases. These association-level data indicate that the metabolic status of the liver microenvironment can have a profound effect on tumor cell capacity to cope with and subsequently outgrow. Intriguingly, the study also identified an increase in the presence of activated NK cells (high GZMB and GNLY expression) in the livers of patients with localized pancreatic cancer. The levels of activated NK cells did not associate with liver recurrence, suggesting that tumor cell capacity to avoid innate immune cell–mediated death was requisite for hepatic metastasis formation.

NK cell responses are driven by recognition and direct cytolysis of tumor cells through secretion of perforin and granzyme and via production of cytokines such as IFNγ and TNFα (10–12). The activation of NK cells is governed by a dynamic balance of signals received from the engagement of numerous activating and inhibiting surface receptors. Inhibitory receptors on NK cells such as killer cell immunoglobulin-like receptors (KIR), leukocyte immunoglobulin-like receptor family B (LILRB) in human, and Ly49 family of receptors in mice, and NKG2A/NKG2C display robust inhibitory effect on NK cell cytolytic function through recognition of classical and nonclassical MHC-I (self-recognition) molecules (13–16). Activating receptors such as NKG2D and natural cytotoxicity receptors promote NK cell effector function by recognizing a wide array of non–MHC-I ligands (10, 11). Not surprisingly, tumor cells downregulate the surface expression of NK cell–activating ligands through various mechanisms, including intracellular retention, shedding surface ligands with metalloproteinases or via exosome secretion, while upregulating inhibitory receptors/ligands to tilt the balance toward evasion of NK cell recognition (17–22).

NK cells make up to 50% of the liver lymphocyte population, and although a mature tumor microenvironment (TME) can suppress function, skew differentiation, and alter phenotype, newly arriving tumor cells face an NK cell population primed to kill (8, 9, 23, 24). We therefore hypothesized the presence of a gene expression program that is actionable prior to or upon arrival that links metabolic plasticity to NK cell escape in order to facilitate subsequent outgrowth. To systematically identify and define candidate genes phenotypically linked to hepatic outgrowth, we conducted an unbiased *in vivo* overexpression screen using two isogenic pancreatic tumor cell lines harboring *KRAS*^{G12D} and *TP53*^{R273H} mutations that differ in capacity to form lesions in the liver.

RESULTS

A cDNA Expression Screen Identifies *GCN1* as a Mediator of Metastatic Outgrowth

To identify genes that may confer coupled metabolic and immunoevasive plasticity, we adopted a previously described cDNA screening strategy and used the mouse liver as a filter (25, 26). To employ the screen, we required cell lines that differ in capacity for hepatic growth. For this, we decided to use pancreatic cancer cells given the well-documented profound metabolic alterations that occur in the pancreatic primary TME, which differ substantially from unaffected organs including the liver, and the tumor's well-described metastatic fitness (27). We used the 4964 cell line derived from a KPC (from *Pdx-1-Cre*, *Kras*^{G12D}, *Trp53*^{R273H}) mouse, which is a clinically relevant model as it recapitulates the various stages seen in human disease and contains a conditional point mutation in *TP53* (*TP53*^{R273H}) and a point mutation in *KRAS* (*KRAS*^{G12D}) commonly found in pancreatic adenocarcinoma (28, 29). Given our desire for isogenic cell lines to employ in the screen, we genetically engineered 4964 cells to stably express an mCherry-luciferase-puromycin cassette to facilitate *in vivo* imaging and selection in antibiotic growth medium. The labeled 4964 cells were then injected into the spleen of mice for dissemination into the liver through the mesenteric circulation and monitored weekly for outgrowth via bioluminescence imaging. The 4964 cells gave rise to discrete lesions in the liver upon splenic injection in 4 weeks. To generate a variant with high outgrowth potential, we excised a visible liver lesion, digested it with trypsin, and after filtration and centrifugation, plated the cells in the presence of puromycin. The cell line obtained from the liver lesion was sorted for mCherry and then further passaged (two cycles) in mice through splenic injection to generate a variant highly enriched with hepatic outgrowth capacity. This clone was labeled as 4964 high outgrowth potential (4964-HOP).

We hypothesized that the ostensibly normal-appearing areas of the liver might contain 4964 tumor cells that lack outgrowth potential and therefore do not produce overt lesions during this timeline. To isolate 4964 cells with poor outgrowth potential, we excised the normal-appearing areas of the liver tissue without any visible lesions at 4 weeks, chopped it into small pieces, and digested the tissue with collagenase. The tissue homogenate containing normal liver populations was filtered, centrifuged, and plated in 2D with puromycin. After 2 weeks, several 4964 tumor colonies grew in the presence of puromycin and were expanded and sorted for mCherry positive cells. These 4964 cells with poor outgrowth capacity in the liver were further passaged (two cycles) in mice through splenic injection to generate the clone 4964 poor outgrowth potential (4964-POP). The general schema of the cell derivation strategy is depicted in Supplementary Fig. S1A. To validate the two variants derived by serial passaging in nude mice, we introduced 4964-HOP or 4964-POP in the liver by splenic injection. Whereas 4964-HOP produced a multitude of visible overt liver metastases by 4 weeks, 4964-POP did not produce visible liver lesions in this timeframe (Fig. 1A; Supplementary Fig. S1B and S1C).

Next, we generated high-complexity retroviral cDNA libraries from size-fractionated mRNA isolated from 4964-HOP as previously described (25, 26). These cDNA libraries were then transduced into 4964-POP cells at a low multiplicity of infection (MOI; MOI = 1), and thereafter these cells were introduced into the liver through injection into the spleen of nude mice. The transduced 4964-POP cells produced a total of 44 macroscopic liver lesions in multiple mice within 6 weeks (Fig. 1B). The macroscopic liver lesions were dissected to isolate clonogenic tumor cells, which were further expanded in selective medium. Following this, genomic DNA was isolated from the tumor cells, and integrated proviral cDNAs were identified by sequencing as documented previously (25). In parallel, 4964-POP cells infected with an empty vector were injected into the spleen of nude mice and did not produce macroscopic liver lesions, indicating that insertional mutagenesis does not appreciably contribute to metastasis in this cell line. The result of the screen is summarized in Supplementary Fig. S1D, and the putative cDNA targets identified by sequencing are listed (Supplementary Table S1).

In line with our hypothesis, the screen unveiled multiple genes with defined roles in metabolic regulation (Fig. 1C) but interestingly did not reveal any genes known to be involved in the regulation of innate immunity. Of the six metabolic regulators identified in the screen, the mRNA expression of *GCN1* and *SFXN1* were highly elevated in primary and metastatic PAAD compared with the normal pancreas (Fig. 1D; Supplementary Fig. S1E). The mRNA expression of the other four regulators was either downregulated in the primary tumor in comparison with the normal pancreas, or was unchanged in metastasis compared with the primary tumor (Supplementary Fig. S1F). However, only mRNA expression of GCN1 was associated with poor survival (Fig. 1E; Supplementary Fig. S1G). Intriguingly, GCN1 expression was also associated with poor survival in other solid tumors (gastric, liver, lung, and sarcoma) in which metastases play a dominant role in limiting patient survival (Supplementary Fig. S1H). This prompted us to investigate the molecular function of GCN1. A review of the available pancreatic cancer sequencing data did not reveal any significant mutations or amplifications in *GCN1* (Supplementary Fig. S1I), although GCN1 protein expression was highly elevated in all the human pancreatic cancer cell lines tested compared to the normal immortalized line, HPNE (Fig. 1F).

To validate a causal role of GCN1 in hepatic outgrowth using immunocompetent mice, we attempted to generate GCN1 CRISPR knockout (KO) cells using an aggressive mouse cell line, KPC177669 (hereafter KPC, containing *KRAS*^{G12D}/*TP53*^{R172H}), which was derived from an autochthonous KPC C57BL/6 mouse. However, our attempts to generate *GCN1* KO cells were not successful, likely because *GCN1* KO cells do not survive, consistent with embryonic lethality of *GCN1* KO mice (30). Instead, we generated stable GCN1 knockdown (KD) cells using two different short hairpins (Fig. 1G). Injection of GCN1 KD cells into the spleen of C57BL/6 mice dramatically abrogated liver lesion formation (Fig. 1H). We reasoned that if GCN1 was important for outgrowth in the liver, it should similarly be important for metastatic outgrowth in the lung, which is also a common site of solid tumor metastases and contains high oxygen tension and robust innate immunity in order to contend with constant pathogen/toxin exposure associated with respiration (31). We therefore injected KPC GCN1 KD cells into the tail vein of C57BL/6 mice for dissemination into the lung, which similarly resulted in a dramatic abrogation of pulmonary lesion formation (Fig. 1I).

Previous studies in budding yeast have indicated a role for GCN1 in activating the integrated stress response (ISR) through its interaction with GCN2, although it plays no known role(s) in circumventing innate immunity (32, 33). To gauge if GCN1 may play a role in mediating immune escape along with a potential role in metabolic stress signaling, we simulated the acute nutrient alterations experienced by cells *in vivo* with *in vitro* reduction in glutamine concentration. Glutamine availability is substantially reduced in murine plasma and liver/lung compared with standard cell culture media, and 4964 cells experienced this reduction immediately upon introduction into the mouse circulation. We altered glutamine levels *in vitro* from 4 mmol/L (supraphysiologic levels used in standard cell culture) to 0.5 mmol/L (average plasma glutamine level, henceforth referred to as physiologic glutamine) to mimic the constraints experienced by cells *in vivo* during our screen and subsequently evaluated the resulting transcriptomes (with and without GCN1 expression). In doing so, we identified downregulation of pathways that support glutathione (GSH) production and amino acid (AA) import and biosynthesis with concomitant upregulation of pathways associated with innate and adaptive immune surveillance with GCN1 KD (Fig. 1J). Thus, GCN1 may couple metabolic reprogramming with immune escape.

GCN1 Regulates Metabolic Homeostasis and Tumor Growth by Activating ATF4

We hypothesized that pancreatic tumor cells utilize GCN1 to cope with acute alterations in nutrient availability and oxygen tension. To investigate, we evaluated the effects of physiologic glutamine on GCN1 signaling in KPC cells.

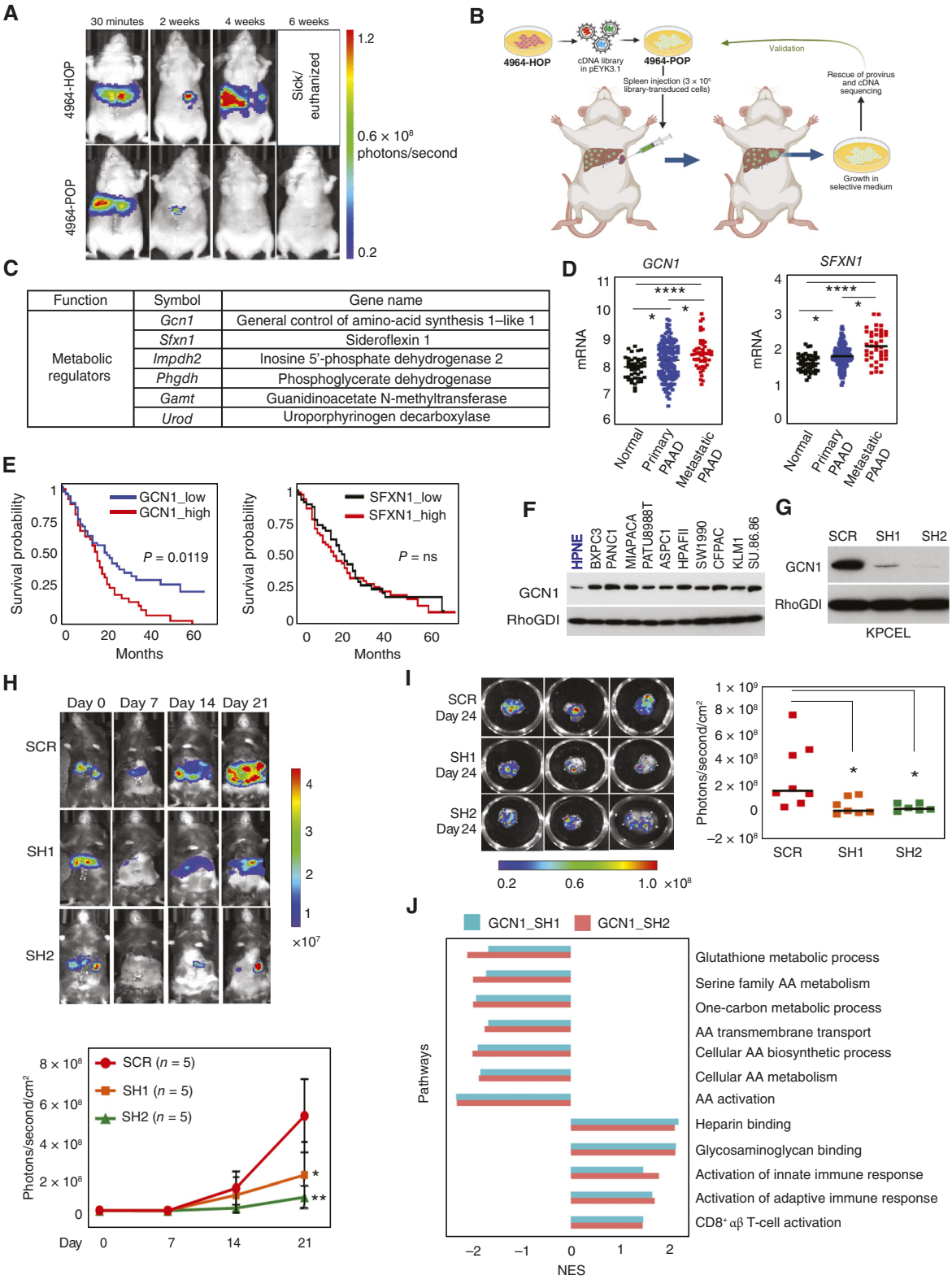

Figure 1. A liver-specific cDNA expression screen identifies GCN1 as a mediator of metastatic outgrowth. **A,** 4964-HOP and 4964-POP cells were injected into the spleen of nude mice, and metastatic outgrowth in the liver was monitored using bioluminescence imaging at 30 minutes, 2 weeks, 4 weeks, and 6 weeks. Representative images of mice. **B,** Design of the retroviral gain-of-function cDNA screen. Retroviral cDNA libraries generated from 4964-HOP cells were transduced into 4964-POP cells. After transduction with 4964-HOP libraries, the 4964-POP cells were injected into the spleen of nude mice and monitored weekly using bioluminescence imaging. (*continued on following page*)

Physiologic glutamine modestly enhanced GCN1 protein expression while strongly inducing the phosphorylation of GCN2 and eIF2α, leading to robust activation of ATF4 (Fig. 2A, lanes 1 and 2). Interestingly, GCN1 KD abolished the phosphorylation of GCN2 and eIF2α and strongly impaired ATF4 activation both at physiologic and supraphysiologic levels of glutamine (Fig. 2A, lanes 3–6). Concordantly, cell proliferation in 2D was dramatically reduced under both conditions, suggesting that GCN1-dependent activation of the ISR drives cell proliferation both at physiologic and supraphysiologic levels of glutamine (Fig. 2B). Previous work in budding yeast has documented that GCN1 interacts with GCN2 at translating ribosomes, leading to its kinase activation (33). We found that GCN1 interacts strongly with GCN2 using *in vitro* GSH transferase (GST) pull-down assay (Supplementary Fig. S2A). Although the transcript levels of GCN1 and GCN2 remained unaltered at differential glutamine levels, GCN2 KD impaired downstream eIF2α phosphorylation and ATF4 expression, mirroring the effect observed with GCN1 KD (Supplementary Fig. S2B and S2C). Importantly, GCN1 expression positively correlated with GCN2 expression, which in turn positively associated with eIF2α expression in PAAD (Supplementary Fig. S2D).

As ATF4 is the major effector molecule of the ISR, we investigated its regulation by GCN1. It is known that upon AA limitation and activation by the ISR, ATF4 translocates to the nucleus to trigger the transcription of genes containing C/EBP-ATF response elements to modulate a wide spectrum of cellular events designed to adapt to stress. If adaptation is unsuccessful, activation of ISR leads to apoptotic cell death (34–36). We observed that *Atf4* mRNA was strongly induced with physiologic glutamine (~3 fold) and this induction was abrogated by GCN1 KD (Fig. 2C). In addition, treatment with the transcriptional inhibitor actinomycin D completely collapsed ATF4 activation at physiologic glutamine levels, suggesting that GCN1-dependent ATF4 induction is completely transcriptional in KPC cells (Fig. 2D). Physiologic glutamine also induced *ATF4* mRNA expression in some human pancreatic cancer cell lines (Supplementary Fig. S2E). Interestingly, physiologic glutamine led to robust phosphorylation of GCN2 and eIF2α and induction of ATF4 protein expression in KLM1 cells, whereas GCN1 KD abrogated ATF4 protein expression (Supplementary Fig. S2F). This suggests that GCN1 drives transcriptional and translational activation of ATF4 in pancreatic cancer cells in response to alterations in glutamine availability. To directly gauge the effects of ATF4 on hepatic outgrowth, we knocked down ATF4 in KPC cells using two specific short hairpins and injected the cells into the spleen of C57BL/6 mice for dissemination into the liver through the mesenteric circulation. ATF4 KD significantly abrogated the formation of liver lesions, mirroring the phenotype seen with GCN1 KD (Fig. 2E; Supplementary Fig. S2G).

To better understand the breadth of metabolic alterations mediated by GCN1 in response to physiologic glutamine, we first reviewed the RNA sequencing (RNA-seq) data for enzymes involved with GSH metabolism and its precursor AAs glycine, glutamate, and cysteine. We identified the serine biosynthetic pathway enzymes PHGDH, PSPH, and PSAT1, which suggests that generated serine and glycine were affected by GCN1 KD (Fig. 2F; ref. 37). Serine is further catabolized by the folate cycle enzymes, ALDH1L2 and MTHFD2, to generate reducing equivalents (NADPH) needed to convert oxidized GSH to its reduced form (38). The enzymes CTH and CBS that produce cysteine through the transsulfuration pathway, and the reversible transaminases BCAT1 and GPT2 that generate glutamate through catabolism of branched chain AAs and alanine, respectively, were significantly altered (39–41). Although GSH precursors are nonessential AAs (NEAA), highly proliferative cells (outgrowing cells) are thought to acquire a portion of these AAs from external sources as the demand exceeds the capacity for endogenous synthesis (42). Not surprisingly, the AA transporters, SLC7A11 and SLC6A9 that mediate the import of cysteine and glycine, respectively, were also significantly affected by KD of GCN1 (Fig. 2G; refs. 43, 44). Additionally, members of the GSH family conjugating enzymes, GSTP1 and GSTK1, which are required for detoxification of reactive electrophiles, and the GSH-degrading enzyme, CHAC1, which maintains intracellular homeostatic balance of GSH, were also altered (45, 46). Furthermore, the expression of SHMT2 and MTHFD1L, two critical enzymes required for mitochondrial–cytoplasmic folate cycle maintenance and therefore production of NADPH, was similarly affected (Fig. 2F; refs. 47, 48). Besides these critical enzymes, other enzymes involved in GSH metabolism through the γ-glutamyl cycle including GCLC and OPLAH were also significantly affected by KD of GCN1 (Supplementary Table S2; ref. 46). Notably, the majority of these GSH-related enzymes are transcriptional targets of ATF4 (35, 49). Not surprisingly, the Ingenuity upstream regulator analysis of differential genes in the GCN1 KD KPC cells predicted *Atf4* to be the most downregulated transcription factor gene (Supplementary Fig. S2H). As expected, RNA-seq data showed that the expression of these metabolic genes and AA transporters was upregulated at physiologic glutamine, which was abrogated by GCN1 KD (Fig. 2F and G). Importantly, the reduction in the expression of these GSH-related genes in

Figure 1. ***(Continued)*** Candidate mediators and drivers of metastatic outgrowth were recovered from macroscopic liver lesions and identified through sequencing. **C,** List of the metabolic regulators identified in the screen. **D,** *GCN1* and *SFXN1* expression across primary and metastatic pancreatic adenocarcinoma (PAAD) compared with the normal pancreas. **E,** Kaplan–Meier OS analysis of *GCN1* and *SFXN1* in pancreatic adenocarcinoma tumors from the Moffitt dataset (95). **F,** Protein expression of GCN1 in human pancreatic cell lines compared with the normal immortalized HPNE (blue) cell line. **G,** KPC cells stably expressing emerald luciferase (KPCEL) were transduced with two different short hairpins (SH1 and SH2) targeting GCN1. Western blots showing reduction in GCN1 protein expression. **H,** Control KPC (SCR) and GCN1 KD (SH1 and SH2) cells were injected into the spleen of syngeneic C57BL/6 mice, and metastatic outgrowth and colonization in the liver were measured using bioluminescence imaging weekly. Top, representative images of mice from each group at specific days; bottom, quantification of liver metastatic outgrowth. Data represent mean ± SD, $n = 5$. **I,** Control KPCEL (SCR) and GCN1 KD (SH1 and SH2) cells were injected via tail vein in syngeneic C57BL/6 mice, and pulmonary outgrowth was measured on day 24 using bioluminescence imaging. Representative images of lungs with bioluminescence signal on day 24. Data represents mean ± SD; $n = 6$. **J,** Gene Ontology signaling pathways affected by GCN1 KD KPC cells grown in DMEM containing 0.5 mmol/L glutamine in comparison with 4 mmol/L glutamine. *P* values were calculated by Student *t* test: *, $P < 0.05$; **, $P < 0.01$; ****, $P < 0.0001$. NES, normalized enrichment score.

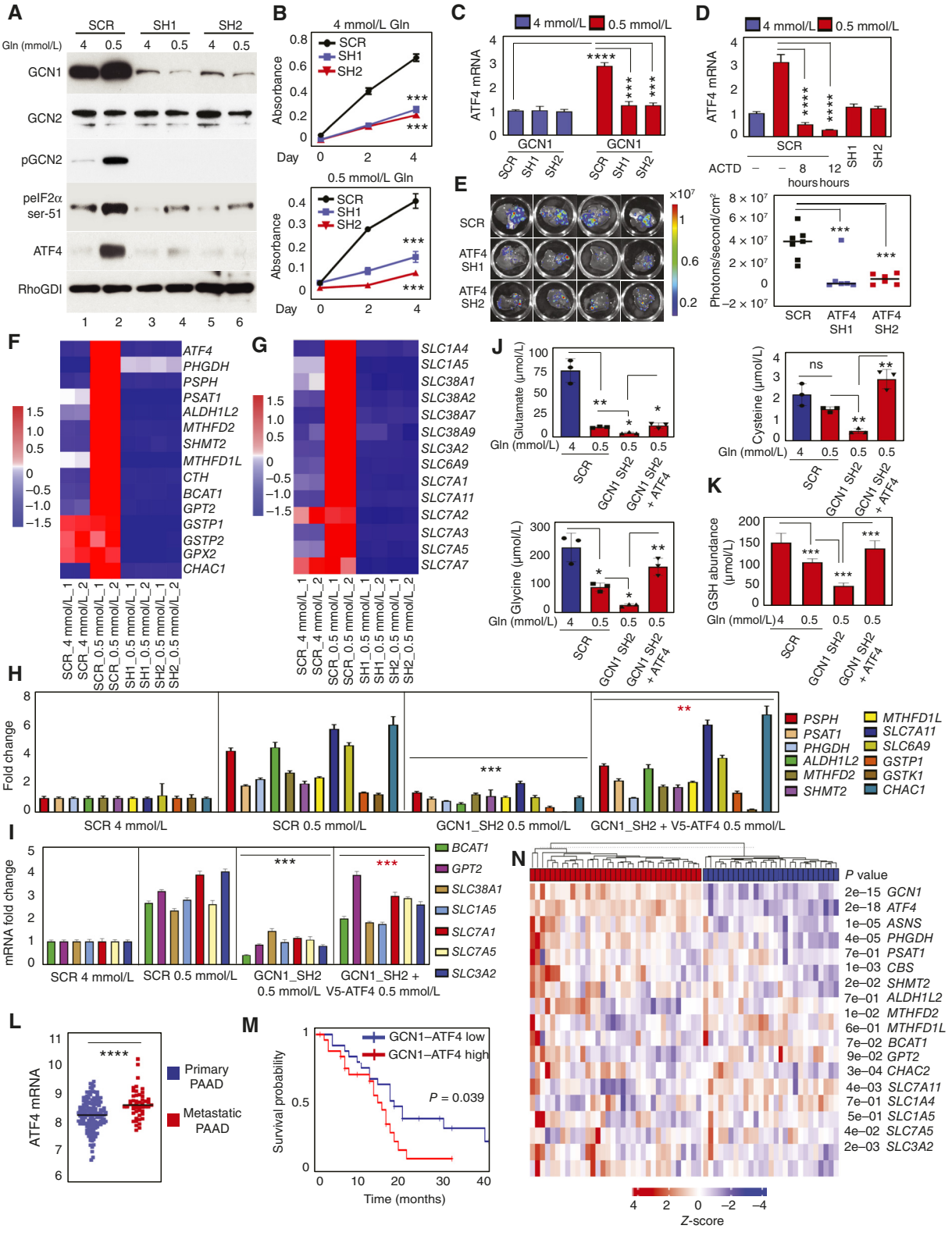

Figure 2. GCN1 drives metastatic growth through activation of ATF4. **A,** KPC control (SCR) and GCN1 KD (SH1 and SH2) cells were grown in DMEM containing either 4 or 0.5 mmol/L glutamine for 24 hours. Cell lysates were subjected to immunoblotting as indicated. **B,** Cell proliferation of KPC control (SCR) and GCN1 KD (SH1 and SH2) cells at 4 or 0.5 mmol/L glutamine using 3-(4,5-dimethylthiazol-2-yl)-2,5-diphenyltetrazolium bromide reagent at indicated days. **C,** *ATF4* mRNA in control (SCR) and GCN1 KD (SH1 and SH2) KPC cells grown at 4 and 0.5 mmol/L glutamine for 24 hours. **D,** *ATF4* mRNA in control (SCR) KPC cells grown at either 4 or 0.5 mmol/L glutamine in the presence and absence of 10 μmol/L actinomycin D (ACTD) for indicated times. (*continued on following page*)

GCN1 KD cells could be rescued by ATF4 expression (Fig. 2H and I; Supplementary Fig. S2I). Accordingly, after 72 hours of growth at physiologic glutamine, we found that GCN1 KD significantly attenuated the intracellular homeostatic abundance of all three precursor AAs required for the biosynthesis of GSH, which could be rescued by ATF4 expression (Fig. 2J). Consequently, GCN1 KD led to a marked decrease in the intracellular levels of GSH at physiologic glutamine, which again could be rescued by the re-expression of ATF4 (Fig. 2K). To evaluate if the lower levels of GSH observed in GCN1 KD cells sensitize to reactive oxygen species (ROS)–induced cell death, we treated KPC cells with the ROS inducer ter-butyl hydrogen peroxide. We observed that ter-butyl hydrogen peroxide treatment at physiologic glutamine induced a significant increase in the endogenous ROS in all cells [Supplementary Fig. S2J (left)]. Intriguingly, GCN1 KD cells were significantly more susceptible to ROS-induced death compared with control cells at physiologic glutamine, and ATF4 expression rescued susceptibility [Supplementary Fig. S2J (right)]. Considering the vast array of metabolic genes downregulated by GCN1-dependent ISR signaling including *Phgdh*, we also looked at the possibility of other four metabolic regulators identified in the screen to determine if they are also regulated by GCN1–ATF4 signaling. We found that the expression of *Urod*, *Gamt*, and *Impdh2* was instead significantly upregulated upon GCN1 KD, whereas *Sfxn1*, which was downregulated by GCN1 KD, was not rescued by re-expression of ATF4, suggesting alternate metabolic pathway regulation of these genes (Supplementary Fig. S2K). These data suggest that tumor cells majorly utilize the GCN1–ATF4 signaling to exert control over the expression of serine biosynthetic pathway, the folate cycle, and the transsulfuration pathway enzymes to buffer the oxidative stress.

In addition to counteracting oxidative stress, outgrowth requires continuous acquisition of essential AAs (EAAs) and NEAAs. We observed that KPC cells cope with 16 hours of physiologic glutamine through transcriptional upregulation of several AA transporters including SLC1A5, SLC7A1, SLC38A1, and SLC3A2, which mediate the uptake of NEAAs, as well as SLC7A5, which is responsible for importing EAAs (Fig. 2G; refs. 50, 51). Interestingly, GCN1 KD largely abrogates this upregulation, which can be rescued by re-expression of ATF4 (Fig. 2G and I). Accordingly, we observed stability of the intracellular levels of all EAAs and NEAAs after 72 hours of physiologic glutamine as measured by mass spectrometry, which was deregulated by GCN1 KD and rescued with ATF4 expression (Supplementary Fig. S2L and S2M). Additionally, we measured L-leucine uptake in KPC cells using a stable isotope (D10, 15N). Cells greatly increased the uptake of L-leucine with 16 hours of physiologic glutamine, which was largely abrogated by GCN1 KD and rescued with ATF4 expression (Supplementary Fig. S2N). We also observed diminished intracellular levels of alpha-ketoglutarate (α-KG) and acetyl-CoA in GCN1 KD cells after 72 hours of growth at physiologic glutamine, which could be rescued by ATF4 expression, suggesting the involvement of GCN1 in regulating α-KG flux through the tricarboxylic acid cycle (TCA) and its role in lipid biosynthesis, respectively (Supplementary Fig. S2O and S2P; refs. 52, 53). The changes in the expression of these enzymes and transporters were also consistent in the human pancreatic cell line KLM1 upon GCN1 KD at physiologic glutamine, demonstrating conservation of a signaling mechanism downstream of GCN1 (Supplementary Fig. S2Q). These data suggest that GCN1–ATF4 signaling–mediated regulation of transporters is a major route of AA assimilation necessary for maintenance of metabolic homeostasis in responses to acute alterations. Concordantly, we found that ATF4 mRNA levels were significantly higher in human metastatic PAAD compared with primary PAAD (Fig. 2L). Moreover, we found that human PAAD tumors expressing higher levels of GCN1 and ATF4 are associated with poor survival and display significantly higher expression of AAs, GSH-related biosynthetic genes, and AA transporters (Fig. 2M and N). Consistent with these observations, ectopic expression of GCN1 in KLM1 cells in which endogenous GCN1 levels were depleted using a short hairpin targeting its 3′ untranslated region (UTR) not only restored the phosphorylation of GCN2 and eIF2α and activated ATF4 expression at physiologic glutamine levels but also restored *in vivo* tumor growth in immunodeficient NOD-SCID IL2Rγ KO mice (Supplementary Fig. S2R and S2S). In aggregate, our data indicate that GCN1 mediates a survival program through ATF4 that couples AA acquisition to redox homeostasis, which endows cells with a growth advantage in response to acute microenvironment alterations.

IMPACT Limits ATF4 Activation through Competitive Inhibition of GCN1

To explore GCN1 regulation, we treated 4964-POP and 4964-HOP cells with physiologic and supraphysiologic levels of glutamine *in vitro*. Intriguingly, we found that GCN1

Figure 2. ***(Continued)*** GCN1 KD (SH1 and SH2) KPC cells were used as the control. **E,** KPCEL control (SCR) and ATF4 KD (SH1 and SH2) cells were injected into the spleen of immunocompetent syngeneic C57BL/6 mice. Left, representative images of livers with bioluminescence signal from each group on day 25; right, metastatic growth quantified using bioluminescence imaging of the liver at day 25. Data represent mean ± SD; $n = 6$. **F,** Heatmap of genes supporting GSH metabolism in control (SCR) and GCN1 KD (SH1 and SH2) KPC cells grown at 4 and 0.5 mmol/L glutamine. **G,** Heatmap of AA transporters in control (SCR) and GCN1 KD (SH1 and SH2) KPC cells grown at 4 and 0.5 mmol/L glutamine. **H** and **I,** RT-qPCR showing the mRNA levels of various metabolic enzymes and AA transporters required for GSH metabolism in KPC control (SCR), GCN1 KD (GCN1_SH2), and GCN1 KD cells stably expressing ATF4 (GCN1_SH2 + V5-ATF4) after growth in DMEM containing either 4 or 0.5 mmol/L glutamine as indicated for 16 hours. Black asterisk denotes a significant decrease between KPC control (SCR, 0.5 mmol/L) and the GCN1 KD (GCN1_SH2, 0.5 mmol/L) group, and red asterisk denotes a significant increase between GCN1 KD (GCN1_SH2, 0.5 mmol/L) and ATF4 rescue (GCN1_SH2 + V5-ATF4, 0.5 mmol/L). **J,** Intracellular abundance of GSH precursors glutamate, glycine, and cysteine in KPC control (SCR), GCN1 KD (GCN1_SH2), and GCN1 KD cells stably expressing ATF4 (GCN1_SH2 + V5-ATF4) after growth in 4 or 0.5 mmol/L glutamine for 72 hours. **K,** Intracellular abundance of GSH in KPC control (SCR), GCN1 KD (GCN1_SH2), and GCN1 KD cells expressing ATF4 (GCN1_SH2 + V5-ATF4) grown at either 4 or 0.5 mmol/L glutamine as indicated for 72 hours. **L,** *ATF4* mRNA expression in primary and metastatic PAAD tumors (95). **M,** Kaplan–Meier survival plot of *GCN1*-high, *ATF4*-high vs. *GCN1*-low, *ATF4*-low expressing PAAD tumors. **N,** PAAD tumors with high mRNA expression of GCN1 and ATF4 positively correlate with the expression of various AAs and GSH metabolic enzymes as well as AA transporters. *P* values calculated by Student *t* test: non significant (ns), $P \geq 0.05$; *, $P < 0.05$; **, $P < 0.01$; ***, $P < 0.001$; ****, $P < 0.0001$. Glutamine (Gln).

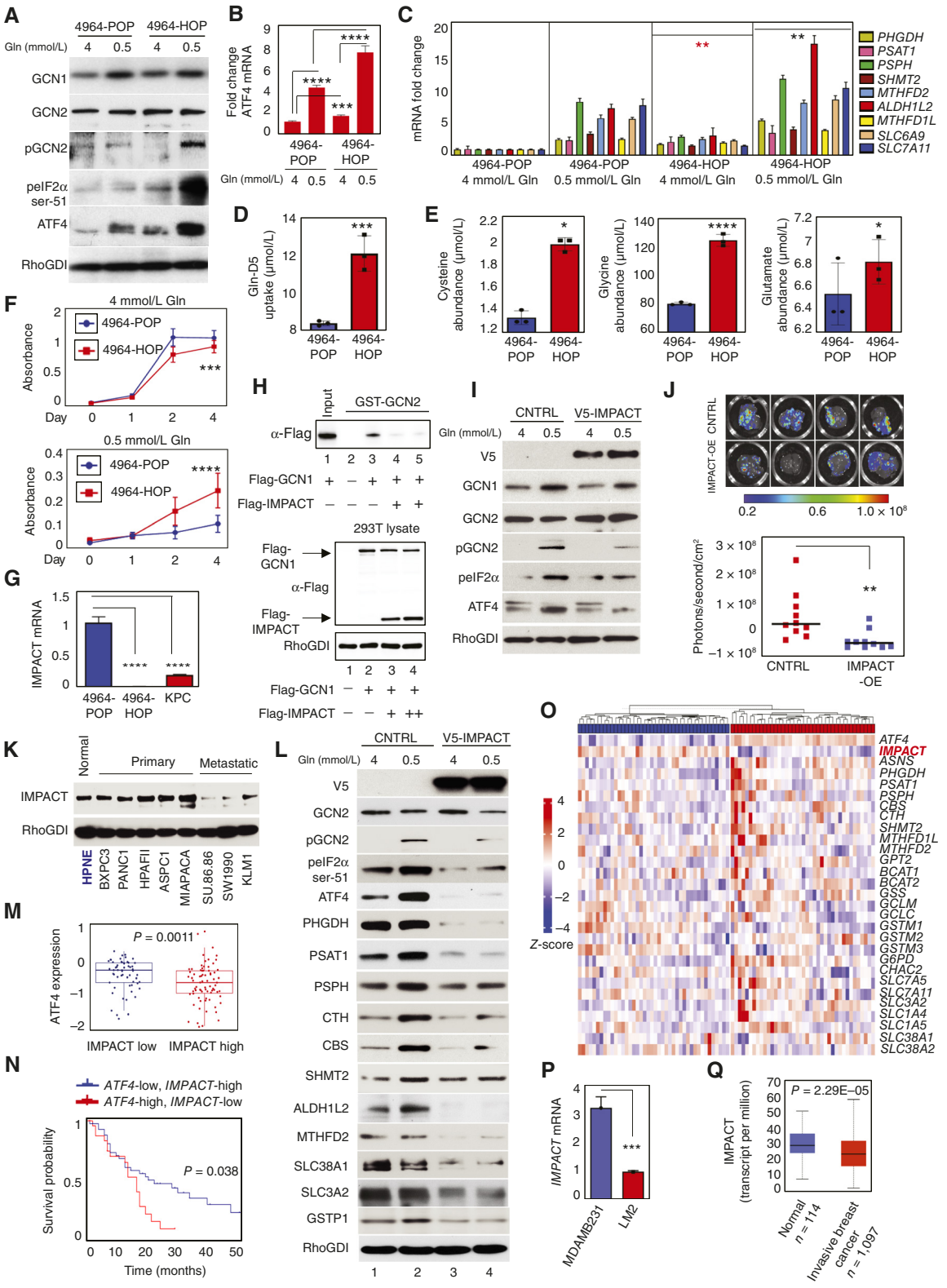

Figure 3. IMPACT limits ATF4 activation through competitive inhibition of GCN1. **A,** 4964-POP and 4964-HOP cells were cultured in DMEM containing 4 or 0.5 mmol/L glutamine for 24 hours, and extracted lysates were subjected to immunoblotting. **B,** *ATF4* mRNA expression in 4964-POP and 4964-HOP cells grown in DMEM containing 4 or 0.5 mmol/L glutamine for 24 hours. **C,** Transcript levels of GSH-related metabolic enzymes assayed using RT-qPCR in 4964-POP and 4964-HOP cells grown in DMEM containing either 4 or 0.5 mmol/L glutamine for 24 hours. Red and black asterisks indicate significant difference at 4 and 0.5 mmol/L glutamine, respectively. (*continued on following page*)

protein expression was similar between the two cell lines, although the phosphorylation of GCN2 and eIF2α with subsequently increased ATF4 expression in response to physiologic glutamine was far more robust in 4964-HOP compared with 4964-POP (Fig. 3A). The increase in ATF4 protein expression reflected proportionally to its increase in mRNA, which was induced twofold higher in 4964-HOP compared with that in 4964-POP (Fig. 3B). Accordingly, 4964-HOP cells demonstrated significantly increased expression of GSH-related biosynthetic genes and AA transport genes with physiologic glutamine compared with 4964-POP cells (Fig. 3C; Supplementary Fig. S3A). Moreover, in comparison with 4964-POP cells, 4964-HOP cells uptake higher levels of glutamine heavy isotope (D5), accumulate higher intracellular levels of GSH-precursor AAs in response to physiologic glutamine, and demonstrate higher intracellular abundance of EAAs (Fig. 3D and E; Supplementary Fig. S3B). Consequently, 4964-HOP cells were able to circumvent the arresting effects of physiologic glutamine and proliferate, wherease 4964-POP cells were susceptible (Fig. 3F). To summarize, 4964-POP cells are unable to circumvent the growth constraints induced by physiologic glutamine despite some induction of GCN1 expression and ostensibly adequate endogenous expression of GCN2.

These observations led us to postulate the presence of novel *GCN1* mutations in 4964-HOP cells that activate the pathway or the presence of an endogenous inhibitor in 4964-POP, which antagonized GCN1 function. cDNA sequencing of *GCN1* from 4964-POP and 4964-HOP cells did not reveal any new mutations (Supplementary Table S3). We therefore subjected 4964-HOP and 4964-POP cells to RNA-seq and examined the transcriptomic differences for candidates. We identified *IMPACT* as the sixth highest expressing gene in 4964-POP cells (Supplementary Table S4). IMPACT has been previously shown to inhibit GCN1-dependent activation of GCN2 in budding yeast and in neuronal cells during AA starvation by binding to the C-terminal RWD-binding domain (RWDBD) of GCN1 (Supplementary Fig. S3C; refs. 54–56). In addition to the RWDBD, GCN1 has 47 HEAT (Huntingtin, Elongation factor 3, A subunit of Protein Phosphatase 2A, and TOR)-repeat domains dispersed throughout its length including three in the RWDBD that serve as a scaffold for higher-order protein–protein and protein–nucleic acid interactions (www.uniprot.org/uniprotkb/Q92616/entry; ref. 57). However, the role of IMPACT in cancer and regulation of GCN1 function has not been investigated. To confirm the RNA-seq results, we evaluated IMPACT expression by RT-qPCR and found significantly abrogated expression in 4964-HOP and KPC cells compared with 4964-POP cells (Fig. 3G). To verify that IMPACT binds GCN1 to prevent its interaction with GCN2, we performed a GST pull-down assay using full-length recombinant GST-GCN2. Specifically, lysates from 293T cells overexpressing Flag-GCN1 or both Flag-GCN1 and Flag-IMPACT were incubated with bead-bound GCN2. 293T lysates from Flag-GCN1 overexpression, but not from overexpression of both Flag-GCN1 and Flag-IMPACT, were able to interact with GCN2 (Fig. 3H). A similar experiment using the RWDBD of GCN1 also yielded identical results (Supplementary Fig. S3D). These data indicate that IMPACT is a competitive inhibitor of GCN1 and causally contributes to the outgrowth phenotype of 4964-POP.

To investigate if IMPACT also plays a role in limiting outgrowth in other pancreatic tumor cells, we overexpressed IMPACT in KPC cells. Stable overexpression of IMPACT in KPC cells strongly inhibited the phosphorylation of GCN2 and eIF2α and impaired ATF4 expression at physiologic glutamine levels, mirroring the effects seen with GCN1 KD (Fig. 3I). Consequently, IMPACT overexpression abrogated liver lesion formation in KPC cells following splenic injection in immunocompetent C57BL/6 mice (Fig. 3J). Identical results were obtained with lung lesions when IMPACT-overexpressing (IMPACT-OE) KPC cells were introduced into the tail vein of immunocompetent C57BL/6 mice (Supplementary Fig. S3E). We next examined the expression of IMPACT in human pancreatic cancer cell lines. Immunoblot revealed that IMPACT expression was variable across the panel but was lowest in metastatic lines SU.86.86, SW1990, and KLM1 (Fig. 3K). We therefore stably overexpressed IMPACT in KLM1 cells and evaluated the effects on downstream pathway activation. IMPACT overexpression prevented the phosphorylation of GCN2 and eIF2α and strongly impaired ATF4 activation both at supraphysiologic and physiologic glutamine levels (Fig. 3L). IMPACT overexpression also inhibited the expression of GSH-related metabolic enzymes and AA transport genes

Figure 3. ***(Continued)*** **D,** Intracellular uptake of stable isotope of glutamine (Gln-D5) in 4964-POP and 4964-HOP cells grown in DMEM for 16 hours. **E,** Intracellular abundance of GSH precursors glutamate, glycine, and cysteine in 4964-POP and 4964-HOP KPC cell lines when grown in DMEM containing 0.5 mmol/L glutamine for 16 hours. **F,** 4964-POP, and 4964-HOP cells were grown in DMEM containing 4 or 0.5 mmol/L glutamine, and cell proliferation was assayed using 3-(4,5-dimethylthiazol-2-yl)-2,5-diphenyltetrazolium bromide at days indicated. Results are represented as mean ± SD ($n = 10$). **G,** mRNA expression of IMPACT in 4964-POP, 4964-HOP, and KPC cells using RT-qPCR. **H,** *In vitro* pull-down assay. Top, full-length human recombinant GST-GCN2 proteins bound to GSH Sepharose beads (lanes 2–5) were incubated with 293T control lysate (lane 2), 293T lysate overexpressing full-length Flag-GCN1 alone (lane 3), and 293T lysate overexpressing Flag-GCN1 together with increasing amounts of Flag-IMPACT (lanes 4–5). Five percent of 293T overexpressing Flag-GCN1 lysate used for the pull-down was used as the input control (lane 1). Binding efficiency was detected using α-Flag antibody. Bottom, expression of Flag-GCN1 and Flag-IMPACT in 293T lysates used in the pull-down assay in a single gel. **I,** KPC-CNTRL and IMPACT-OE (V5-IMPACT) cells were grown in DMEM containing 4 and 0.5 mmol/L glutamine for 16 hours, and lysates were subjected to immunoblotting with antibodies indicated. **J,** KPC-CNTRL and IMPACT-OE (V5-IMPACT) cells were injected into the spleen of immunocompetent C57BL/6 mice, and metastatic outgrowth and colonization in the liver were measured using bioluminescence imaging at day 25. Top, representative images of the liver with bioluminescent signal at day 25; bottom, metastatic outgrowth quantified. **K,** IMPACT expression across human pancreatic cell lines in comparison with the normal hTERT-immortalized pancreas cell line HPNE (blue). **L,** KLM1-CNTRL and IMPACT-OE (V5-IMPACT) cells were grown in DMEM containing 4 or 0.5 mmol/L glutamine for 24 hours. Lysates were subjected to immunoblotting by antibodies shown. **M,** Boxplot showing *ATF4* expression in *IMPACT* high– vs. *IMPACT* low–expressing pancreatic adenocarcinoma (PAAD) tumors. **N,** Kaplan–Meier survival between *ATF4*-high, *IMPACT*-low vs. *ATF4*-low, *IMPACT*-high expressing PAAD tumors. **O,** *IMPACT* expression inversely correlates with the expression of *ATF4* and ATF4 gene targets in PAAD tumors. **P,** *IMPACT* mRNA expression in MDAMB231 and lung metastatic variant LM2 cell lines. **Q,** *IMPACT* mRNA levels in normal breast tissue and invasive breast cancer (The Cancer Genome Atlas/UALCAN dataset]. *P* values by Student *t* test: *, $P < 0.05$; **, $P < 0.01$; ***, $P < 0.001$; ****, $P < 0.0001$. Gln, glutamine.

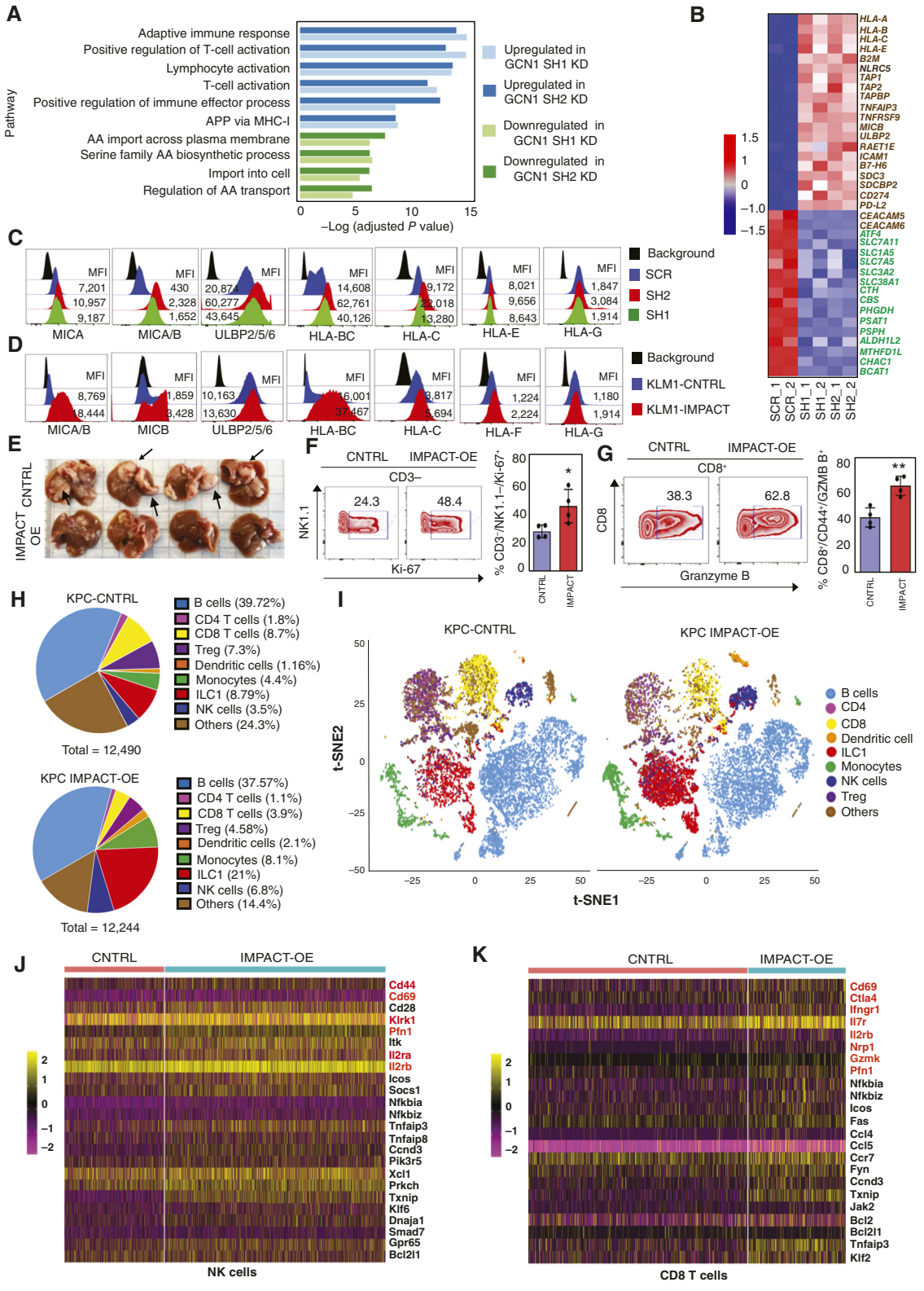

Figure 4. IMPACT abrogates GCN1-mediated immune cell evasion. **A,** Gene Ontology enrichment analysis of significantly altered molecular pathways in GCN1 KD KLM1 cells. **B,** Heatmap of immunomodulatory genes (brown), and AA/GSH metabolism genes (green) altered in GCN1 KD KLM1 cells. **C** and **D,** Surface expression of NKG2D ligands (MICA, MICB, and ULBP2/5/6) and MHC-I (classical and nonclassical) in KLM1 control (SCR) and GCN1 KD (SH1 and SH2) cells (left); KLM1 control (KLM1-CNTRL) and IMPACT-OE (KLM1-IMPACT) cells (right). Mean fluorescent intensity (MFI) values for samples provided. **E,** Liver images from C57BL/6 WT mice after intrasplenic injection of control and IMPACT-OE KPC cells at day 25. (*continued on following page*)

compared with control cells, irrespective of glutamine concentration (Fig. 3L, lanes 1 and 3). Accordingly, IMPACT-OE KLM1 cells have reduced expression of AA transporters, showed reduced ability to uptake L-leucine stable isotope (D10, 15N), and have significantly lower intracellular GSH abundance (Supplementary Fig. S3F–S3H). Consequently, IMPACT overexpression abrogated liver lesion formation following splenic injection in athymic nude mice (Supplementary Fig. S3I). To verify this relationship in human PAAD, we categorized tumors as IMPACT high or IMPACT low using median expression and found that *ATF4* mRNA expression was significantly lower in tumors with high IMPACT expression (Fig. 3M). Additionally, we found that PAAD tumors expressing high levels of *ATF4* and low levels of *IMPACT* were associated with significantly abbreviated survival (Fig. 3N) and display higher expression of genes involved in GSH metabolism and AA transport (Fig. 3O). Considering that our preliminary RNA-seq data indicate that GCN1 may play a role in activation of innate and adaptive immune responses, we injected IMPACT-OE KPC cells into the tail vein of immunodeficient NOD-SCID IL2Rγ KO mice that lack both NK and T cells and evaluated pulmonary lesion formation. Overexpression of IMPACT significantly reduced lung lesion formation in these severely immunodeficient mice (Supplementary Fig. S3J), suggesting that the inhibition of metabolic plasticity alone (independent of any effects on immune evasion) is sufficient to suppress outgrowth capacity.

To evaluate if IMPACT plays a similar role in metastatic outgrowth in another isogenic cell line pair, we choose the well-characterized breast cancer cell line MDA-MB-231 and its lung metastatic variant LM2 (58). Exposure of LM2 cells to physiologic glutamine levels robustly induced the phosphorylation of GCN2 and eIF2α, and expression of ATF4 with consequent activation of its downstream targets (Supplementary Fig. S3K). However, phosphorylation of GCN2 and expression of ATF4 and its targets were only mildly enhanced in MDA-MB-231 cells under physiologic glutamine levels, whereas phosphorylation of eIF2α, although expressed at a higher basal level compared with LM2 cells, remained unchanged (Supplementary Fig. S3K). The inhibition in the full activation of GCN2 phosphorylation and ATF4 expression in MDA-MB-231 cells at physiologic glutamine levels hinted the presence of IMPACT. RT-qPCR confirmed that MDA-MB-231 cells express significantly higher levels of IMPACT (>3 fold) compared to LM2 cells (Fig. 3P). Analysis of The Cancer Genome Atlas dataset also showed significant loss of IMPACT expression in invasive breast cancer compared with normal tissue (Fig. 3Q). Furthermore, as expected, IMPACT overexpression in LM2 cells blocked ISR pathway activation and pulmonary lesion formation in comparison to control LM2 cells or MDA-MB-231 cells (Supplementary Fig. S3L–S3N). Recently, MIRO2, a small Ras superfamily GTPase, has been shown to bind GCN1 and activate GCN1–ATF4 signaling in prostate cancer (59). This prompted us to investigate the status of MIRO2 in pancreatic and breast cancers. Intriguingly, we found MIRO2 expression to be significantly upregulated in the same metastatic PAAD and invasive breast cancer datasets in which IMPACT expression is lost (Supplementary Fig. S3O and S3P). Together, these data suggest that loss of IMPACT expression with concomitant gain in the expression of MIRO2 leads to hyperactivation of the GCN1–ATF4 signaling and is a general evolutionary survival mechanism to buffer oxidative stress and metabolic growth constraints associated with tumor progression and metastasis.

IMPACT Abrogates GCN1-Mediated Immune Cell Evasion

To begin to examine the role of GCN1 in immune regulation, we carried out RNA-seq analysis in KLM1 cells. With GCN1 KD, we observed strong upregulation of pathways associated with immune cell activation [lymphocyte activation and antigen processing and presentation (APP) via MHC class I (MHC-I) pathways; Fig. 4A; Supplementary Fig. S4A] and a strong increase in the expression of genes that control tumor-immune responses (Fig. 4B). We validated the changes in immune genes at the transcript level and surface expression using RT-qPCR and FACS, respectively. Among the tumor-immune responsive genes, we observed significant upregulation of the expression of various NKG2D activation ligands, including MHC-I polypeptide–related sequence A/B, and the ULBP family of proteins (Fig. 4C; Supplementary Fig. S4B; ref. 60). The ligand B7-H6, recognized by natural cytotoxicity receptor 3 (NKp30) on NK cells, was also significantly upregulated by KD of GCN1 (Supplementary Fig. S4B; ref. 61). Natural cytotoxicity receptors including NKp46, NKp30, and NKp44 recognize abnormal or altered expression of proteoglycans like syndecans on the tumor cell surface and activate NK cell cytotoxicity (10, 61). Abnormal expression of other glycoproteins like cell adhesion molecule 5/6 (CAECAM5/6) has been shown to inhibit NK cell effector function (62–64). Intriguingly, we found increased expression of some syndecans (SDC3 and SDCBP2) and decreased expression of cell adhesion molecules 5/6 (CAECAM5/6) in GCN1 KD cells (Fig. 4B). We also observed significant upregulation of the expression of various classical and nonclassical HLAs, β2 microglobulin, antigen processing and transport molecules (TAP1/2), and peptide transport and loading molecule Tapasin (TPSN; Fig. 4C; Supplementary Fig. S4C and S4D). In the presence of proper co-stimulation in the TME, the expression of these APP machinery genes on tumor cells is crucial to elicit CD8 T-cell responses through engagement with

Figure 4. ***(Continued)*** Tumor lesions are shown by arrows. **F** and **G,** Leukocytes isolated from the livers of mice that received control or IMPACT-OE KPC cells were stained with immune-specific antibodies. NK cell proliferation was assayed using Ki-67$^+$ staining after gating CD3$^-$ population and percentage of CD8$^+$ T effector memory cells (CD8$^+$/CD62L$^-$/CD44$^+$; gated on CD8$^+$) positive for granzyme B (CD8$^+$/CD44$^+$/GZMB$^+$). **H** and **I,** Leukocytes isolated from the liver of mice that received either control or IMPACT-OE KPC cells at day 25 were subjected to single-cell RNA-seq. Pie chart and t-SNE plot show the percentage distribution of various immune cells in the liver seeded with control and IMPACT-OE cells. **J** and **K,** Heatmaps of NK and CD8 cell clusters from **H** and **I**. Activation markers are highlighted in bold red. *P* values calculated by Student *t* test: *, $P < 0.05$; **, $P < 0.01$. CNTRL, control; MICA/B, MHC-I polypeptide–related sequence A/B; Treg, regulatory T cells; t-SNE, t-distributed stochastic neighbor.

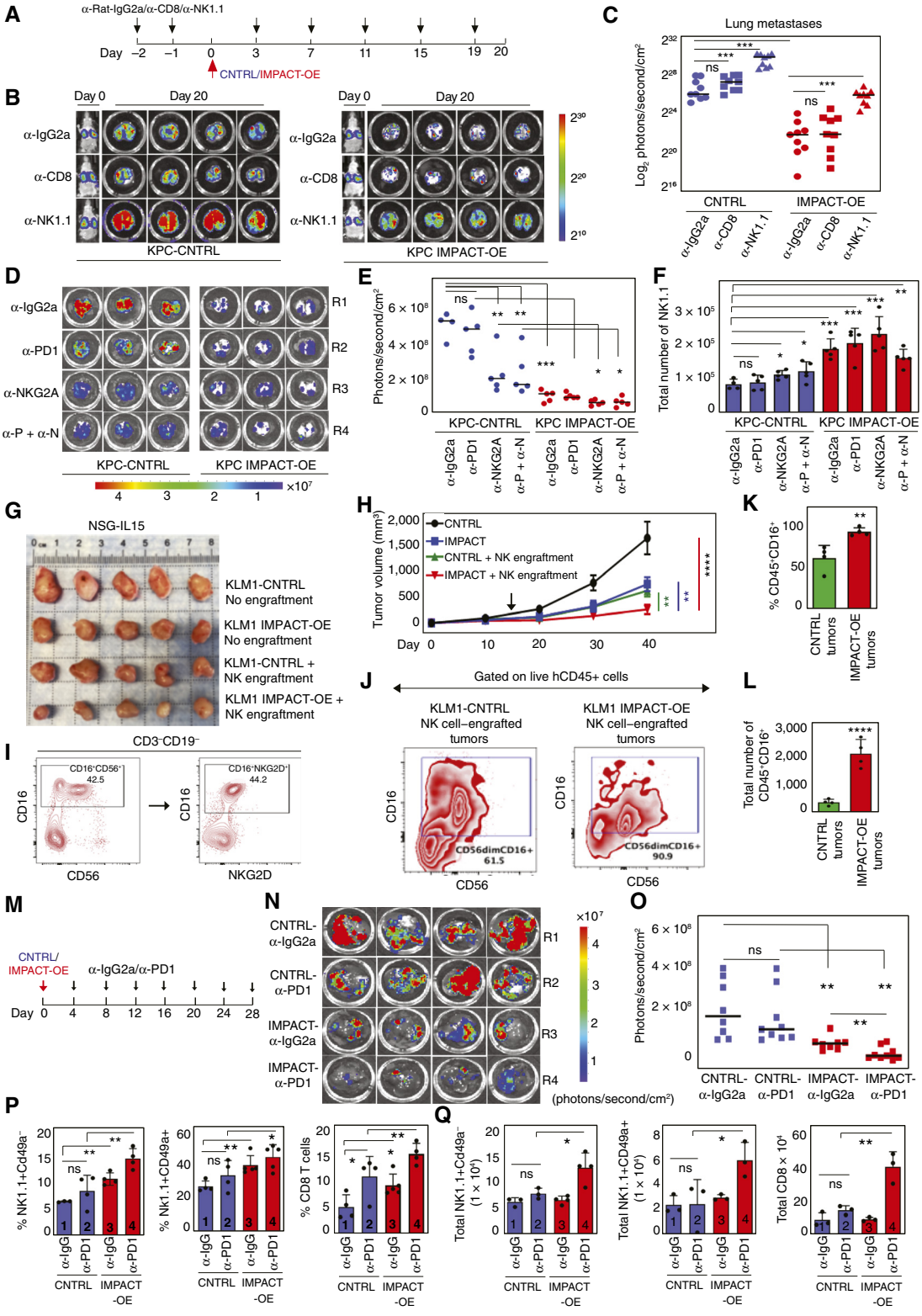

Figure 5. NK cells eliminate IMPACT-expressing tumor cells through NKG2D recognition. **A,** Pulmonary outgrowth assay by immune cell depletion. Schema showing days (black arrows) on which C57BL/6 immunocompetent mice were intraperitoneally dosed with 200 μg/mouse control α-IgG2a, or α-CD8 (CD8 depletion), or α-NK1.1 (NK depletion) antibodies. Tumor cell (KPC-CNTRL or KPC IMPACT-OE) was injected through the tail vein on day 0 (red arrow). **B,** Bioluminescent lung images of mice at day 20 that received control IgG2a or α-CD8 or α-NK depletion antibodies in the KPC-CNTRL (left) or KPC IMPACT-OE (right) cohort. Whole-body bioluminescent images at day 0 within 30 minutes of tumor cell injection. **C,** Pulmonary outgrowth was quantified using bioluminescent imaging at experimental endpoint. (*continued on following page*)

antigen-specific T-cell receptors (TCR; ref. 65). Interestingly, the negative regulators of T-cell responses, PD-L1 and PD-L2, were also upregulated on tumor cells (Supplementary Fig. S4D and S4E; refs. 66, 67).

To identify the plausible mechanism behind these widespread changes in the immunoregulatory genes, we performed the Ingenuity upstream regulator analysis in KLM1 cells with GCN1 KD. Surprisingly, the cytokines TNFα and IFNγ were predicted to be among the top 10 regulators that could be driving the observed gene expression changes (Supplementary Fig. S4F). Although the expression of both TNFα and IFNγ were barely detectable in control tumor cells, GCN1 KD modestly upregulated them (Supplementary Fig. S4G). Additionally, the expression of MHC-I regulator, NLRC5, was also significantly upregulated by KD of GCN1 (Supplementary Fig. S4H). Importantly, loss of expression of IFNγ, TNFα, and NLRC5 is a major mechanism of immune escape and immune checkpoint resistance in metastatic cancers (68–70). As IMPACT can inhibit GCN1, we examined if blocking GCN1 function by expression of IMPACT can mimic the gene expression changes observed with GCN1 KD. Indeed, overexpression of IMPACT in human KLM1 cells significantly upregulated the expression of NKG2D ligands, MHC-I (both classical and nonclassical), APP genes, and NLRC5 together with checkpoint ligands PD-L1/PD-L2, as well as TNFα and IFNγ (Fig. 4D; Supplementary Fig. S4I–S4L). Stable overexpression of IMPACT in mouse KPC cells also induced similar upregulation in the expression of mouse MHC-I and NK ligands (Supplementary Fig. S4M).

To evaluate the effects of these immune-related gene alterations on outgrowth potential, IMPACT-OE or control KPC cells were introduced into the liver via splenic injection in syngeneic C57BL/6 mice. Whereas an abundance of hepatic lesions was observed with the introduction of control KPC cells into the mouse liver, the livers of mice seeded with IMPACT-OE cells had significantly fewer lesions, with some livers demonstrating almost no lesions at all (Fig. 4E). To identify the changes in the immune repertoire within these livers, we isolated hepatic leukocytes and analyzed them via FACS. We found significant enrichment in the percentage, but not total number, of NK cells ($CD3^-/NK1.1^+$) positive for Ki-67 and effector $CD8^+$ T cells positive for granzyme B, suggesting that introduction of IMPACT-OE tumor cells in the liver robustly activated the cytolytic activity of NK and effector $CD8^+$ T cells (Fig. 4F and G; Supplementary Fig. S4N). To further characterize the immune subsets, we performed single-cell RNA-seq analysis on isolated hepatic leukocytes. We analyzed a total of 12,490 cells from the KPC control (KPC-CNTRL) group and 12,244 cells from the KPC-IMPACT-OE group (Fig. 4H). Although the relative cellular composition of B cells was found to be similar, we found significantly increased frequencies of innate lymphoid cells [innate lymphoid cell group 1(ILC1)– $NK1.1^+/Cd49a^+$] and NK cells ($NK1.1^+/Cd49a^-$) in the IMPACT-OE leukocyte population compared to control KPC leukocyte population (Fig. 4H and I). Similar to conventional NK cells, ILC1s are liver-resident NK cells that produce IFNγ and exhibit robust cytotoxic activity against tumor cells (71–73). Other innate cells including dendritic cells and monocytes also showed increased frequencies in the IMPACT-OE group. Surprisingly, we observed decreased frequencies of adaptive immune T cells including CD8, CD4, and Tregs with IMPACT-OE cells (Fig. 4H and I). Differential gene expression analysis of NK, CD8, and ILC1 cell clusters on a single-cell basis as shown by heatmaps revealed increased expression of NK, CD8, and ILC1-specific activation markers including perforin, granzyme, Il2ra, and Il2rb (Fig. 4J and K; Supplementary Fig. S4O). Accordingly, pathway analysis in these cell clusters showed significant upregulation of TNFα–NF-κB and IL2–STAT5 proliferative signaling pathways (Supplementary Fig. S4P and S4Q; refs. 74–76). Collectively, these data suggest that GCN1 KD or IMPACT overexpression increases tumor immunogenicity and activates both innate and adaptive antitumor immune responses in mice.

NK Cells Eliminate IMPACT-Expressing Tumor Cells through NKG2D Recognition

To elucidate the immune cell populations that recognize and eliminate IMPACT-OE tumor cells, we depleted NK cells or $CD8^+$ T cells through intraperitoneal injection of neutralizing antibodies prior to and following the introduction of tumor cells into the lung via tail-vein injection in C57BL/6 mice (Fig. 5A). As expected, IMPACT-OE KPC cells abrogated pulmonary lesion formation (Fig. 5B, top images and Fig. 5C). Surprisingly, depletion of NK cells but not $CD8^+$ T cells led to large increases in pulmonary lesion formation with the introduction of control or IMPACT-OE KPC cells (Fig. 5B, bottom images and Fig. 5C). Depletion of $CD8^+$ T cells

Figure 5. ***(Continued)*** **D,** Bioluminescent lung images of C57BL/6 RAG KO mice on day 28 that received KPC-CNTRL or IMPACT-OE cells through the tail vein after treatment with α-PD1 (200 μg/mouse), or α-NKG2A (200 μg/mouse) alone, or in combination every 3 days from the day of tumor cell injection until the experimental endpoint. **E,** Quantification of pulmonary metastases using bioluminescence imaging of lungs on day 28 between KPC-CNTRL and IMPACT-OE cohorts in the presence and absence of α-PD1, α-NKG2A, or combination (α-P + α-N) treatment. **F,** Leukocytes isolated from the lungs of RAG KO mice were stained with α-NK1.1 and analyzed using FACS. Total number of NK cells in each group provided. **G** and **H,** CNTRL and IMPACT-OE KLM1 cells were subcutaneously implanted on the upper right flank of NSG-Tg (Hu-IL15) mice and allowed to develop tumors for 2 weeks. On day 14 (black arrow), NK cells ($CD16^+CD56^+$) isolated from a healthy donor expressing NKG2D (**I**) were retro-orbitally injected into the tumor-bearing mice ($10{\times}10^6$ cells/mouse). Tumor images at the endpoint (day 40), and tumor volume at different days are shown. **J–L,** Tumors resected from the right flank of KLM1-CNTRL and KLM1 IMPACT-OE mice that were adoptively engrafted with healthy donor NK cells were mechanically dissociated at day 40, and tumor-infiltrating leukocytes were isolated and stained with α-CD45, α-CD16, and α-CD56; percentage and total number of NK cells ($CD45^+CD16^+CD56$dim) gated on live $hCD45^+$ cells. **M,** Schematic showing days (black arrows) on which C57BL/6 immunocompetent mice were intraperitoneally dosed with control α-IgG2a or α-PD1 antibodies (200 μg/mouse). KPC-CNTRL or IMPACT-OE cells were injected through the spleen on day 0 (red arrow). **N,** Representative bioluminescent liver images of mice on day 28 that received either KPC-CNTRL or IMPACT-OE cells via the spleen and were either treated with isotype control antibody (α-IgG2a) or antibody targeting PD1 (α-PD1) at a concentration of 200 μg/mouse. **O,** Quantification of liver metastatic growth from bioluminescent liver images on day 28. **P** and **Q,** Leukocytes isolated from the livers from **N** were stained with immune-specific antibodies, and live cells were analyzed using FACS. Percentage and total number of NK (NK1.1), ILC1 (CD49a), and CD8 T cells in control and IMPACT-OE cohorts that received isotype antibody (α-IgG2a) or α-PD1. *P* values calculated by Student *t* test: *ns* $P \geq 0.05$; *, $P < 0.05$; **, $P < 0.01$; ***, $P < 0.001$; ****, $P < 0.0001$. CNTRL, control.

had no visible effect and mirrored the lung lesion formation observed in the control groups that received isotype IgG2a antibodies (Fig. 5B, middle images and Fig. 5C). Interestingly, we observed liver lesion formation following tail-vein injection in mice without NK cells (Supplementary Fig. S5A and S5B, bottom livers), indicating the robustness of lesion formation in the absence of NK cells and highlighting the important role of NK cells in limiting multiorgan outgrowth. It should be noted that depletion of NK cells also depletes ILC1s as all ILC1 cells express NK1.1.

Activated and exhausted NK cells express PD1, and its engagement by PD-L1+ tumor cells suppresses NK cell–mediated antitumor immunity (77). Similarly, activated and exhausted NK cells express the inhibitory NKG2A receptor and its engagement with nonclassical MHC-I molecule HLA-E (human) or Qa-1 (mice) potently suppresses NK cell–mediated antitumor activity (14, 78). Interestingly, both α-PD1 and α-NKG2A have been shown to independently augment NK cell activation by blocking the engagement of PD1 and NKG2A receptors on NK cells with PD-L1 and Qa-1/HLA-E ligands expressed on tumor cells, respectively (14, 77, 78). To investigate if NK cell activity could be further enhanced pharmacologically beyond that observed with the introduction of IMPACT-OE tumor cells, we utilized the checkpoint inhibitors α-PD1 and α-NKG2A in RAG KO mice, which lack T cells. Control KPC or IMPACT-OE KPC cells were introduced into the lung of RAG KO mice via tail-vein injection with or without α-PD1 and α-NKG2A antibodies. IMPACT-OE KPC cells alone dramatically abrogated lung lesion formation compared with control KPC cells when treated with isotype IgG2a control antibody (Fig. 5D, R1 and Fig. 5E). Interestingly, α-NKG2A treatment alone and in combination with α-PD1 but not α-PD1 alone significantly abrogated pulmonary growth in the KPC-control group (Fig. 5D, R2 vs. R3/R4 and Fig. 5E). In the IMPACT-OE group, the addition of α-NKG2A or α-PD1 alone or in combination did not further abrogate pulmonary lesion formation (Fig. 5D and E, R1 vs. R2/R3/R4). However, the abrogation of pulmonary lesion formation was significantly more dramatic in IMPACT-OE KPC cells with and without α-NKG2A and α-PD1 treatment than the control KPC cells receiving the same treatment. To investigate the plausible cause for the abrogation of pulmonary growth in the IMPACT-OE group, we isolated the pulmonary leukocytes from these RAG KO mice and analyzed the NK cell population. We found significantly increased total NK cell abundance in the lungs of the IMPACT-OE group compared with the KPC-control group (Fig. 5F). We also observed significantly higher abundance of NK cells in the KPC-control group that received α-NKG2A alone or α-PD1 and α-NKG2A combined but not in the group that received α-PD1 alone. This suggests that α-NKG2A can more effectively induce pulmonary NK cell activation than α-PD1 and that IMPACT-OE KPC cells are more susceptible to NK cell killing because of their enhanced immunogenicity compared with the control KPC cells. Although the total NK cell abundance was clearly and significantly elevated on day 28, we did not observe any significant change in the percentage of NK cells either in the KPC-control or IMPACT-OE group that received α-PD1 or α-NKG2A. This could be likely due to the attainment of NK-mediated immune homeostasis (10–12).

To determine if the NKG2D receptor on NK cells mediates the prevention of pulmonary lesion formation with the introduction of IMPACT-OE tumor cells, we depleted endogenous NK cells actively expressing the NKG2D receptor through intraperitoneal injection of NKG2D neutralizing antibodies (Supplementary Fig. S5C). Depletion of NKG2D-expressing NK cells markedly increased pulmonary lesion formation with the introduction of control KPC cells or IMPACT-OE KPC cells into the lungs via tail-vein injection (Supplementary Fig. S5D and S5E). To test if introduction of NK cells can eliminate or restrict established tumors, we performed adoptive transfer of human NK cells expressing the NKG2D receptor from a healthy donor into NSG-hIL15 transgenic mice harboring subcutaneous tumors at day 14 (79). Whereas the engraftment of NK cells into mice bearing control tumors resulted in some growth restriction, transfer of NK cells into mice bearing IMPACT-OE tumors resulted in substantial growth restriction (Fig. 5G–I). Furthermore, tumor-infiltrating leukocytes isolated from NK cell–engrafted tumors and gated on live hCD45$^+$ cells showed a marked increase in the frequency and abundance of CD45$^+$CD16$^+$ NK cells in IMPACT-OE tumors compared with the control tumors (Fig. 5J–L). These results indicate that IMPACT overexpression unveils tumor cells for recognition and elimination by NK cells through NKG2D-dependent ligand–receptor interactions, consistent with prior work demonstrating that mice deficient in NKG2D expression are defective in tumor surveillance (80).

To further test if NK cells can mount similar antitumor immune response upon IMPACT overexpression in other poorly immunogenic tumor cell lines in addition to KPC, we overexpressed IMPACT in the B16F10 melanoma cell line that is commonly used as a highly aggressive model for murine immunotherapy studies. Stable overexpression of IMPACT enhanced the expression of murine NKG2D ligands (MULT-1 and RAET1A) as well as the expression of murine MHC-I molecules (H2-Db and H2-Kb; Supplementary Fig. S5F and S5G). As expected, intravenous injection of IMPACT-OE B16F10 cells through the tail vein in both C57BL/6 WT and C57BL/6 RAG KO mice led to complete abrogation of pulmonary lesions (Supplementary Fig. S5H), again highlighting the role of IMPACT in eliciting NK-dependent antitumor immune responses. Consistent with the ability of NKG2D ligands to augment antitumor NK cell responses, we found that 4964-HOP cells significantly downregulate the expression of several NKG2D ligands to escape NK cell immune surveillance (Supplementary Fig. S5I). Consequently, we also observed downregulation of surface expression of mouse MHC-I in these cells (Supplementary Fig. S5J). Similar to the human pancreatic cell line KLM1, stable overexpression of IMPACT in the human colorectal cell line SW480 also upregulated the expression of various NKG2D stress ligands and the ligand B7-H6 for the NKp30 receptor as well as the expression of various HLAs (Supplementary Fig. S5K–S5M). Likewise, the breast cancer metastatic variant LM2 cells, which have low IMPACT expression compared with its parental line MDA-MB-231, also show significantly reduced endogenous expression of NK ligands and MHC-I expression (Supplementary Fig. S5N and S5O). Taken together, these data indicate that IMPACT-dependent regulation of NK ligands plays a critical role in innate immune surveillance and tumor progression to metastasis.

Human pancreatic adenocarcinoma is a poorly immunogenic tumor that does not respond to immune checkpoint blockade (ICB) (81). Tumor cell–intrinsic factors have been documented to shape the tumor immune landscape and influence the outcome of immunotherapy (82). As IMPACT-OE KPC tumor cells activated the cytolytic activity of effector CD8$^+$ T cells when injected in C57BL/6 mice via the spleen (Fig. 4G and K), we examined if expression of IMPACT can augment the efficacy of α-PD1 checkpoint inhibition in KPC cells. For this, IMPACT-OE KPC cells or control cells were introduced into the liver via splenic injection followed by intraperitoneal injection of either α-IgG2a or α-PD1 every 4 days until experimental endpoint (Fig. 5M). Although the expression of IMPACT alone significantly abrogated metastatic outgrowth as expected, the administration of α-PD1 in the IMPACT-OE group further reduced metastatic outgrowth (Fig. 5N and O). Additionally, analysis of leukocytes isolated from the liver demonstrated a significant increase in the frequency and abundance of NK (NK1.1$^+$Cd49a$^-$), ILC1 (NK1.1$^+$/CD49a$^+$), and CD8$^+$ T cells in the IMPACT-OE group that received α-PD1 compared to the control group that also received α-PD1 (Fig. 5P and Q, bar 2 and 4). Collectively, these data suggest that IMPACT overexpression can robustly augment metabolic stress–induced tumor immunogenicity to engage antitumor innate and adaptive immune responses, rendering resistant cells susceptible to checkpoint blockade.

Nuclear GCN1 Stabilizes HNRNPK, Leading to Immune Escape

Although the increased expression of TNFα and INFγ upon GCN1 KD or IMPACT overexpression may explain the gene expression changes observed in MHC-I and APP machinery, it does not explain the widespread changes observed in the expression of NK ligands. To gain insights into the mechanism, we conducted an endogenous GCN1 immunoprecipitation from KPC whole-cell lysate followed by mass spectrometry to identify the interacting partners of GCN1. Among the top hits were mitotic spindle protein KIF11, the DNA repair protein RAD50, and the nucleic acid–binding protein HNRNPK (Supplementary Fig. S6A). Intriguingly, RAD50 and HNRNPK are nuclear proteins, whereas GCN1 has been predominantly reported as a cytoplasmic protein residing in close association with ribosomes. Whereas RAD50 plays a very specific and defined role in DNA double-strand break repair, HNRNPK plays a more widespread role in gene regulation by affecting transcription, RNA stability, splicing, and translation (83–87). Subcellular extracts from normal and pancreatic tumor cell lines indicated that around 20% of GCN1 resides in the nucleus where HNRNPK is predominantly localized (Supplementary Fig. S6B). Intriguingly, the algorithm NLStradamus predicted a moderately strong nuclear localization signal (NLS) in GCN1 (score: 0.7; 70% probability; Supplementary Fig. S6C; ref. 88). Furthermore, immunoprecipitation of HNRNPK from nuclear lysate of KPC cells showed strong interaction with GCN1, confirming that GCN1 interacts with HNRNPK in the nucleus (Supplementary Fig. S6D). Interestingly, GCN1 KD lysates from KLM1 cells showed reduced HNRNPK protein levels without any alteration in the transcript, indicating that GCN1 may regulate HNRNPK protein stability (Fig. 6A and B). As expected, the stability of HNRNPK is substantially reduced (>50%) after 12 hours of cycloheximide treatment in the absence of GCN1 (Fig. 6C). This suggests that GCN1 executes a nuclear function by maintaining the stability of HNRNPK. Not unexpectedly, HNRNPK protein levels are elevated across all pancreatic tumor cell lines compared with the normal immortalized HPNE cells, although transcript levels do not correlate with protein expression at least in MIAPACA and KLM1 cell lines (Supplementary Fig. S6E).

Like *GCN1*, *HNRNPK* KO is embryonically lethal (89). To investigate if HNRNPK KD can mimic the immunophenotype seen with GCN1 KD, we generated doxycycline-inducible HNRNPK KD KLM1 cells. As shown, doxycycline treatment reduced endogenous HNRNPK protein levels, whereas the mRNA expression of NK-activating ligands, checkpoint proteins PD-L1 and PD-L2, and MHC-I molecules, APP genes, and their regulators TNFα, IFNγ, and NLRC5 all increased concomitantly (Fig. 6D; Supplementary Fig. S6F–S6I). The changes in the mRNA expression of NK ligands and MHC-I genes were also reflected on the cell surface (Fig. 6E). To examine the *in vivo* outgrowth effects of these gene expression changes, we generated stable HNRNPK KD KPC cells using short hairpin RNA (shRNA) and confirmed the cell surface changes described above (Fig. 6F and G). Introduction of HNRNPK KD KPC cells in the liver via splenic injection demonstrated significant abrogation of liver metastatic growth compared with control KPC cells in C57BL/6 mice (Fig. 6H; Supplementary Fig. S6J), mimicking the phenotype observed with GCN1 KD. To examine changes in the immune cells after the introduction of tumor cells in the liver with or without HNRNPK KD, we isolated the leukocytes from the liver on day 28 and analyzed the immune cells using flow cytometry. We observed a significant increase in the percentage of activated NK cells (NK1.1+Cd49a$^-$) positive for Ki-67$^+$ and ILC1 (NK1.1+CD49a$^+$) as well as in effector CD8$^+$ T cells (CD44$^+$CD69$^-$Ki-67$^+$) compared to control cells without alteration in their total numbers (Fig. 6I; Supplementary Fig. S6K). Analogous to IMPACT-OE, HNRNPK KD augments both innate and adaptive immune responses.

HNRNPK is a poly-C–binding protein and is known to regulate 3′-end pre-mRNA transcription termination and stability through binding to the cytosine-rich sequences (90–92). We therefore predicted an enrichment of poly-C sequences in the 3′-UTRs of GCN1 KD transcriptomes. Indeed, we found that the density of poly-C content in the 3′-UTRs is significantly higher in GCN1 KD transcripts compared with the control (Fig. 6J). Additionally, we used Transite, a computational motif-based platform that nominates RNA-binding proteins motifs, which are overrepresented in the 3′-UTRs of a gene expression dataset (93). Analysis of GCN1 KD transcripts using Transite demonstrated enrichment of HNRNPK-binding motifs in the 3′-UTRs of GCN1 KD transcriptomes and predicted HNRNPK as the top regulator (Fig. 6K; Supplementary Table S5). To evaluate, we inserted the 3′-UTRs for several immunomodulatory genes altered by GCN1 expression downstream of a dual-luciferase reporter. Insertion of the 3′-UTR sequences alone modestly decreased the reporter activity, indicating the presence of destabilizing elements

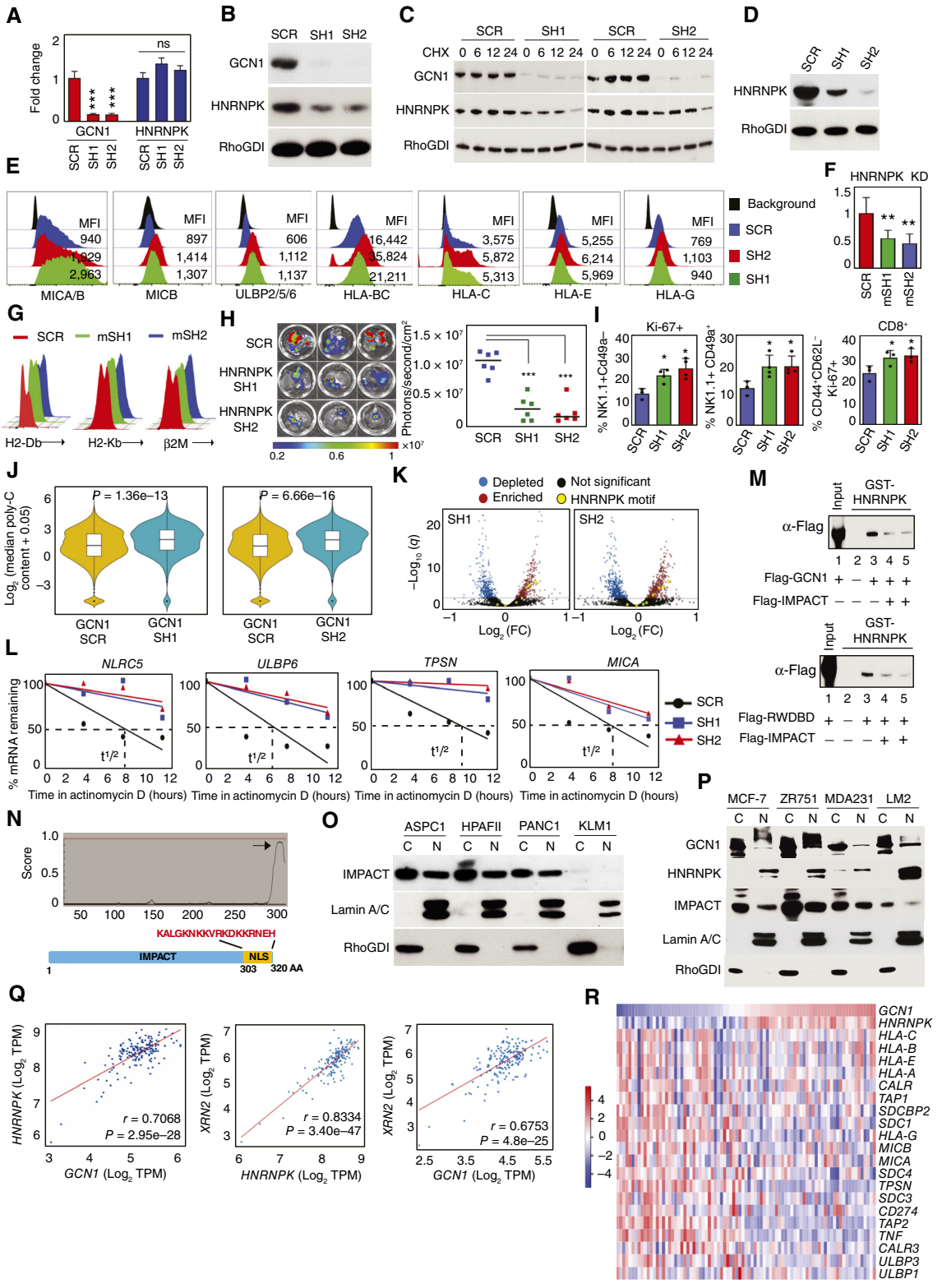

Figure 6. Nuclear GCN1 stabilizes HNRNPK leading to immune escape. **A,** RT-qPCR showing mRNA levels of HNRNPK in GCN1 KD KLM1 cells. **B,** Western blots showing HNRNPK protein levels in GCN1 KD KLM1 cells. **C,** Western blots showing HNRNPK protein stability in GCN1 KD (SH1 and SH2) and control (SCR) mouse KPC cells after treatment with 50 μg/mL cycloheximide (CHX) for 24 hours. **D,** Western blots showing HNRNPK KD in human KLM1 cells using two different doxycycline-inducible short hairpins (SH1 and SH2) after treatment with 20 μg/mL doxycycline for 96 hours compared with control (SCR). **E,** Surface expression of NKG2D ligands and MHC-I (classical and nonclassical) in HNRNPK KD KLM1 cells. **F,** HNRNPK KD in mouse KPC cells using two different shRNAs. **G,** Surface expression of mouse MHC-I in HNRNPK KD KPC cells. (*continued on following page*)

in the 3′-UTR. The reporter activity was further suppressed in the presence of HNRNPK, suggesting destabilization of luciferase transcript by HNRNPK (Supplementary Fig. S6L). Consequently, we also observed an increased half-life of the immune transcripts in HNRNPK KD samples compared to control KLM1 cells when grown in the presence of actinomycin D (Fig. 6L). These data suggest that GCN1-HNRNPK impairs tumor cell immunogenicity to facilitate immune escape. To this end, we speculated that IMPACT would disrupt this interaction to cause an increase in the expression of immune genes as has been shown in Supplementary Fig. S4I–S4M. Accordingly, we found that the binding of full-length GCN1 (Flag-GCN1: top panel) or the RWD domain of GCN1 (Flag-RWDBD: bottom panel) to recombinant HNRNPK is completely lost in the presence of IMPACT using a GST pull-down assay (Fig. 6M). This led us to hypothesize that IMPACT must reside in the nucleus to disrupt the GCN1–HNRNPK interaction. Indeed, the NLStradamus algorithm (88) predicted a strong NLS sequence (score: 0.9; 90% probability; Fig. 6N). Subcellular fractionation and immunoblot analysis in the nuclear and cytoplasmic lysates demonstrated that like GCN1, around 20% to 30% of endogenous IMPACT resides in the nucleus of pancreatic and breast tumor cell lines (Fig. 6O and P). As expected, IMPACT expression was completely lost in the metastatic pancreatic KLM1 cells. Also, IMPACT expression was substantially reduced in the metastatic LM2 breast cancer cells in both the nuclear and cytoplasmic fractions compared with its parental MDA-MD-231 cell line. A similar percentage of IMPACT was also observed in the nucleus when overexpressed in KLM1 cells (Supplementary Fig S6M). Surprisingly, we also observed reduced expression of HNRNPK in the nuclear fraction of IMPACT-OE cells, suggesting that HNRNPK stability is dependent on GCN1 binding (Supplementary Fig. S6M). Furthermore, although HNRNPK KD in human KLM1 cells did not alter the phosphorylation of GCN2 and eIF2α or ATF4 activation at physiologic glutamine levels, some ATF4 target genes involved in GSH metabolism were significantly upregulated, whereas some were significantly downregulated and many others remained unaltered upon HNRNPK KD (Supplementary Fig. S6N and S6O). This suggests that besides immunomodulatory genes, HNRNPK regulates other metabolic pathways/genes independently of ATF4. To further narrow down the mechanism by which HNRNPK regulates innate immune function, we performed endogenous immunoprecipitation of HNRNPK in the nuclear fraction of KLM1 cells and identified the nuclear exoribonuclease XRN2 (Supplementary Fig. S6P). XRN2 has been recently shown to cause transcription termination by interacting with HNRNPK (91). We first validated the interaction of XRN2 and HNRNPK in the nuclear fraction of KLM1 cells (Supplementary Fig. S6Q). Intriguingly, KD of XRN2 in KLM1 cells led to significant upregulation of several NKG2D ligands, the ligand B7-H6 for the NKp30 receptor, the expression of various classical and nonclassical HLAs, β2 microglobulin, APP genes (*TAP1*), peptide transport and loading gene *TPSN*, and expression of *PD-L1*, mimicking the phenotype observed with both GCN1 and HNRNPK KDs (Supplementary Fig. S6R–S6T). In human PAAD tumors, the expression of *GCN1*, *HNRNPK*, and *XRN2* is upregulated, with *HNRNPK*- and *XRN2*-expressing tumors associated with poor survival (Fig. 6Q; Supplementary Fig. S6U). Additionally, PAAD tumors expressing higher levels of *GCN1* and *HNRNPK* display lower expression of immune genes involved in innate and adaptive immune responses (Fig. 6R; Supplementary Fig. S6V). Collectively, these data suggest that GCN1 drives a transcriptional program that mediates immune escape through HNRNPK.

Expression of IMPACT Is Lost through Genomic Deletion and Epigenetic Silencing

Given that IMPACT governs the expression of nutrient acquisition and immune response genes that enable cells to cope with microenvironmental derangements and subvert the host immune surveillance leading to outgrowth, we hypothesized that IMPACT loss facilitates metastasis. To begin, we investigated if IMPACT loss is sufficient to activate the ISR pathway using cell lines. For this, we generated CRISPR-Cas9 KO of IMPACT in 4964-POP cells and confirmed the loss of expression by RT-qPCR (Supplementary Fig. S7A). We found

Figure 6. ***(Continued)*** **H,** KPC control (SCR) and HNRNPK KD (SH1 and SH2) cells were injected via the spleen in immunocompetent C57BL/6 mice, and liver metastatic outgrowth was scored using bioluminescence imaging on day 28. Left, representative liver images with bioluminescent signals; right, quantification of metastatic outgrowth. **I,** Leukocytes isolated from the livers on day 28 from **H** were stained with immune-specific antibodies. Percentage of NK cells positive for Ki-67 (NK1.1-Ki-67$^+$), ILC1 (Cd49a$^+$), and effector CD8 T cells (CD8$^+$CD44$^+$Cd69$^-$) in control (SCR) and HNRNPK KD groups (SH1 and SH2). **J,** Violin plots showing enrichment of poly-C (cytosine) content in the 3′-UTR transcripts from control and GCN1 KD KLM1 cells. **K,** *K-mer*–based transcript set motif analysis using Transite algorithm on GCN1 KD 3′-UTR transcripts from KLM1 cells. **L,** mRNA stability of immune transcripts in HNRNPK KD (SH1 and SH2) KLM1 cells compared with control (SCR) after treatment with actinomycin D (20 μg/mL) for indicated timepoints. mRNA levels of the indicated targets were determined using RT-qPCR. **M,** *In vitro* GST-HNRNPK pull-down assay. Top, full-length human recombinant GST-HNRNPK proteins bound to GSH Sepharose beads (lanes 2–5) were incubated with 293T control lysate (lane 2), 293T lysate overexpressing full-length Flag-GCN1 (lane 3), and 293T lysate overexpressing Flag-GCN1 together with increasing amounts of Flag-IMPACT (lanes 4–5). Bottom, full-length human recombinant GST-HNRNPK protein bound to GSH Sepharose beads (lanes 2–5) were incubated with 293T control lysate (lane 2), 293T lysate overexpressing the Flag-RWDBD of GCN1 (lane 3), and 293T lysate overexpressing Flag-RWDBD of GCN1 together with increasing amounts of Flag-IMPACT (lanes 4–5). Five percent of 293T overexpressing Flag-GCN1 lysate used for the pull-down assay was used as the input control (lane 1). Binding of Flag-GCN1 to GST-HNRNPK was detected uisng α-Flag antibody. **N,** Nuclear localization signal (NLS) prediction using NLStradamus in IMPACT. The predicted NLS sequence is highlighted in red. Black arrow indicates probability score. **O,** Distribution of IMPACT in the cytoplasmic and nuclear fractions of human pancreatic cancer cells. Lamin A/C and RhoGDI were used as nuclear and cytoplasmic controls, respectively. **P,** Distribution of GCN1, IMPACT, and HNRNPK in the cytoplasmic and nuclear fractions of human breast cancer cells. Lamin A/C and RhoGDI were used as nuclear and cytoplasmic controls, respectively. **Q,** Expression of *GCN1*, *HNRNPK*, and *XRN2* positively correlates with each other in The Cancer Genome Atlas pancreatic cancer dataset (www.oncodb.org). **R,** Pancreatic adenocarcinoma tumors with high expression of *GCN1* and *HNRNPK* negatively correlate with the expression of numerous NK activation ligands, MHC-I (classical and nonclassical), APP molecules, and other immunomodulatory genes (95). *P* values calculated by Student *t* test: *ns* $P \geq 0.05$; *, $P < 0.05$; **, $P < 0.01$; ***, $P < 0.001$. β2M, β2 microglobulin; C, cytoplasmic control; MFI, mean fluorescent intensity; MICA, MHC-I polypeptide–related sequence A; N, nuclear control; TPM, transcripts per million.

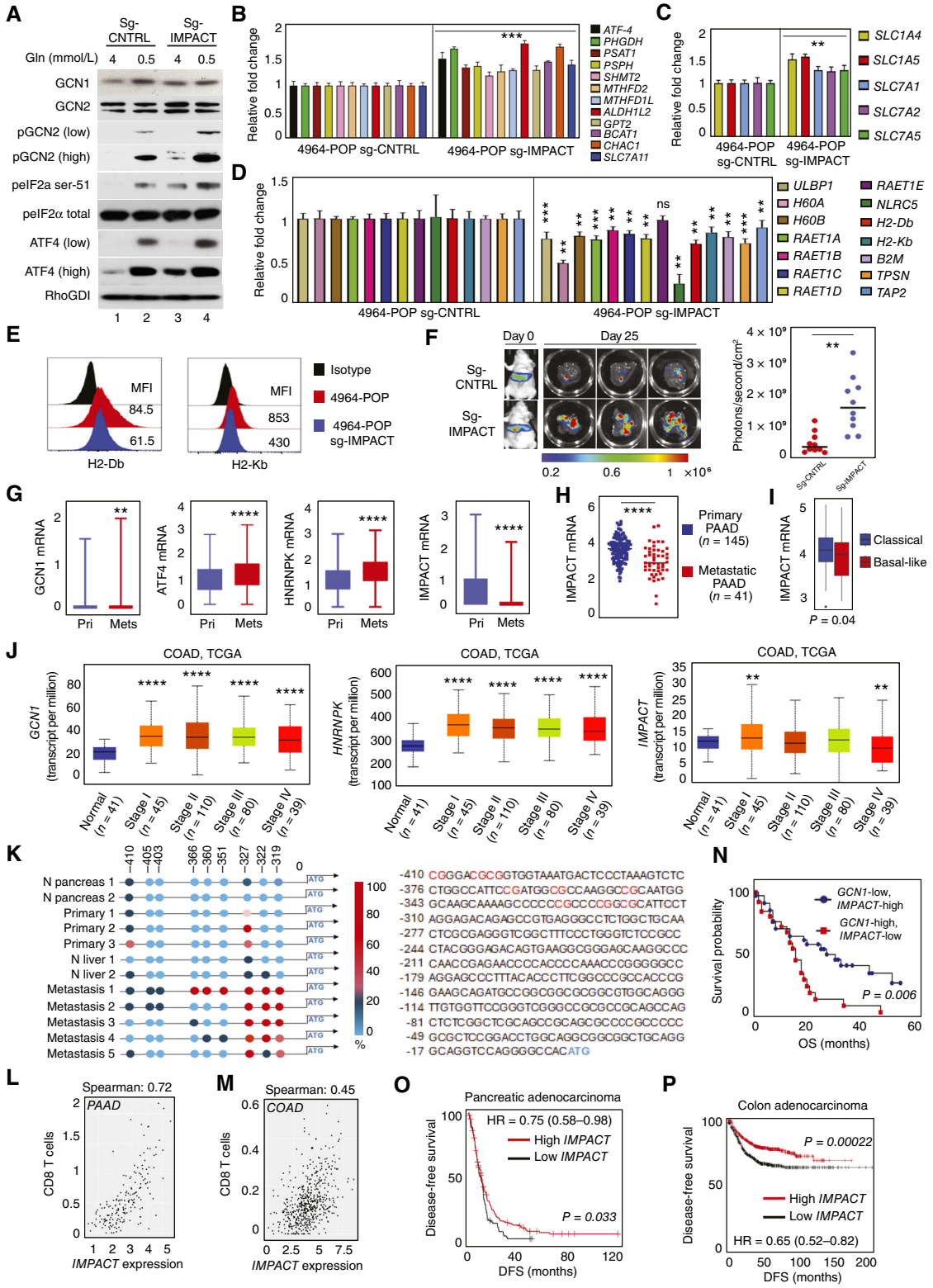

Figure 7. Expression of IMPACT is lost through genomic deletion and epigenetic silencing. **A,** Control (Sg-CNTRL) and IMPACT KO (Sg-IMPACT) 4964-POP cells were grown in DMEM containing 4 or 0.5 mmol/L glutamine for 24 hours, and lysates were subjected to immunoblotting with antibodies indicated. **B** and **C,** mRNA expression of *ATF4*, GSH-related metabolic enzymes, and AA transporters in control (sg-CNTRL) and IMPACT KO (Sg-IMPACT) 4964-POP cells. **D,** mRNA expression of mouse NK ligands, MHC-I, MHC-I regulator, and APP molecules in control (sg-CNTRL) and IMPACT KO (Sg-IMPACT) 4964-POP cells. **E,** Surface expression of mouse MHC-I in control (sg-CNTRL) and IMPACT KO (Sg-IMPACT) 4964-POP cells. (*continued on following page*)

that IMPACT KO 4964-POP cells more robustly phosphorylate GCN2 and eIF2α and upregulated ATF4 expression with physiologic glutamine compared with 4964-POP control cells (Fig. 7A, lanes 2 and 4). Intriguingly, IMPACT KO activated the pathway at 4 mmol/L glutamine as indicated by the increased phosphorylation of GCN2 (high exposure) and eIF2α and ATF4 (high exposure) expression (Fig. 7A, lanes 1 and 3). Not surprisingly, IMPACT KO 4964-POP cells increase the expression of GSH-related genes and AA transporters by RT-qPCR at 4 mmol/L glutamine compared with 4964-POP control cells (Fig. 7B and C). Accordingly, we found that IMPACT KO 4964-POP cells significantly increased the intracellular abundance of GSH and the GSH precursor AAs glutamate, glycine, and cysteine, and demonstrated increased uptake of glutamine heavy isotope (D5) compared to control 4964-POP cells (Supplementary Fig. S7B–S7D). Consistent with the ability to uptake more AAs, IMPACT KO 4964-POP cells also demonstrated increased intracellular abundance of αKG and acetyl-CoA (Supplementary Fig. S7E and S7F). Accordinglly, IMPACT KO 4964-POP cells exhibited significantly reduced expression of mouse MHC-I (H2-Db and H2-Kb) and MHC regulator NLRC5, APP genes (*TAP2* and *TPSN*), and various NK activation ligands (Fig. 7D and E). As expected, IMPACT KO 4964-POP cells formed abundant hepatic lesions after introduction into the liver via splenic injection in athymic nude mice (Fig. 7F).

To evaluate IMPACT expression in human tumors, we analyzed publicly available single-cell data obtained from the tumors of 16 patients with localized or metastatic PAAD (94). A total of 3,587 primary epithelial tumor cells and 5,037 metastatic epithelial tumor cells from the liver and omental lesions were analyzed. As compared with PAAD cells in primary tumors, PAAD cells in metastatic tumors demonstrated significantly lower expression of *IMPACT* with concomitantly significantly higher expression of *GCN1*, *ATF4*, and *HNRNPK* (Fig. 7G). Moreover, the expression of *IMPACT* positively correlated with the expression of MHC-I, APP genes, and NK ligands, whereas it negatively correlated with ATF4, AA transporters, and some GSH-related metabolic enzymes (Supplementary Fig. S7G). We also examined bulk transcriptomic data from primary and metastatic PAAD tumors and found that IMPACT expression was significantly downregulated in metastases compared with primary tumors (Fig. 7H; ref. 95). Furthermore, human PAAD has been classified into two transcriptomic subtypes referred to as classical and basal-like, the latter being associated with poor survival (96). We found that *IMPACT* expression was significantly higher in the classical subtype compared with the basal subtype (Fig. 7I). To evaluate *IMPACT* expression in a second gastrointestinal adenocarcinoma with a propensity for liver and lung metastases, we evaluated TCGA data for colorectal cancer. We found that the *GCN1* and *HNRNPK* transcript levels were significantly elevated compared with those in the normal colon/rectum and that *IMPACT* expression was substantially lower with metastatic disease (stage IV) compared with early-stage disease (stage I, which is associated with recurrence rates <5%; Fig. 7J). We also utilized tumor samples obtained from the operating room of a patient undergoing a combined colon (primary) and liver (metastasis) resection. Western blot analysis using tumor lysates demonstrated a modest increase in the expression of GCN1 and HNRNPK and a significant decrease in expression of IMPACT in the liver metastases compared to the primary tumor (Supplementary Fig. S7H). Transcript analysis using RT-qPCR demonstrated a significant downregulation of NK activation ligands, MHC-I, and APP molecules in the liver metastases compared with the primary tumor (Supplementary Fig. S7I).

To examine if tumor cells dispense IMPACT expression through mutation(s) and chromosomal loss, we examined the Genomic Data Commons portal (www.gdc.cancer.gov). Whereas somatic mutations in *IMPACT* were insignificant (0.03%–0.05%) across tumor types, we observed significant genomic losses of *IMPACT* in different tumor types with the highest levels of deletion seen in rectal adenocarcinoma (READ, 74%), testicular germ cell tumors (TGCT, 69%), and colorectal adenocarcinoma (COAD, 51%; Supplementary Fig. S7J). Genomic deletion of *IMPACT* was also observed in pancreatic adenocarcinoma (PAAD, 24%). In the absence of genomic deletion, epigenetic silencing of alleles largely contributes to loss of gene expression. With loss of heterozygosity (LOH), epigenetic silencing of the second allele is a common mechanism to eliminate gene expression. Interestingly *GATA6*, which is localized to 18q11.2 along with *IMPACT*, regulates the expression of PDX1, which controls pancreas development and has been shown to be epigenetically silenced in the basal-like subtype of PAAD (96–98). These observations led us to hypothesize that tumor cells may also downregulate *IMPACT* expression through epigenetic mechanisms. To begin evaluating, we treated 4964-HOP, 4964-POP, KPC, and KLM1 cells with 5′-Azacytidine in combination with

Figure 7. ***(Continued)*** **F,** Control (Sg-CNTRL) and IMPACT KO (Sg-IMPACT) 4964-POP cells were injected into the spleen of athymic nude mice, and metastatic outgrowth in the liver at day 25 were determined using bioluminescence imaging. Right, metastatic outgrowth quantified from the bioluminescent signal in the liver. **G,** mRNA expression of *GCN1*, *ATF4*, *HNRNPK*, and *IMPACT* in single-cell data of tumors obtained from localized (primary) and metastatic (liver and omentum) PAAD. **H,** Expression of *IMPACT* in primary and metastatic PAAD tumors (95). **I,** Box plot showing the expression of *IMPACT* in classical and basal-like subtypes of PAADs. **J,** mRNA expression of *GCN1*, *HNRNPK*, and *IMPACT* in The Cancer Genome Atlas (TCGA) colon adenocarcinoma (COAD) dataset obtained from UALCAN (https://ualcan.path.uab.edu). **K,** Schematic showing the degree and extent of *IMPACT* promoter methylation in two normal liver tissue (N liver), two normal pancreatic tissue (N pancreas), three primary PAAD tumors (Primary 1, 2, and 3), and five PAAD liver metastases (Metastasis 1, 2, 3, 4, and 5; left). The predicted human CpG island from UCSC Genome Browser was amplified using specific primers spanning the genomic region, and specific cytosine base methylation was identified using MiSeq. Each circle represents a cytosine base in the CpG island, and the degree of methylation in each cytosine base is color-coded. The position of the CpG islands (dinucleotides) relative to the start codon (blue) in the *IMPACT* promoter are highlighted in red (right). **L** and **M,** Correlation of *IMPACT* expression with CD8 T-cell abundance and perforin activity in pancreatic (PAAD, TCGA) and colorectal (COAD, TCGA) adenocarcinomas, respectively. **N,** Kaplan–Meier survival plot of *GCN1*-high, *IMPACT*-low vs. *GCN1*-low, *IMPACT*-high PAAD tumors (95). **O** and **P,** High expression of *IMPACT* predicts higher disease-free survival in pancreatic and colon adenocarcinomas. *P* values calculated by Student *t* test: ns, $P \geq 0.05$; *, $P < 0.05$; **, $P < 0.01$; ***, $P < 0.001$; ****, $P < 0.0001$. Gln, glutamine; Mets, metastatic; MFI, mean fluorescent intensity; Pri, primary.

romidepsin (broad spectrum HDAC inhibitor). Treatment with 5′-azacytidine alone, or in combination with romidepsin but not romidepsin alone, significantly upregulated *IMPACT* expression in 4964-HOP, whereas 5′-azacytidine treatment alone induced significant upregulation of *IMPACT* expression in KPC and KLM1 cells (Supplementary Fig. S7K). Under similar treatment conditions, the expression of *IMPACT* in 4964-POP cells was only mildly affected in comparison with the other pancreatic cell lines. Importantly, 4964-HOP and KPC cells demonstrated heavy promoter methylation compared with 4964-POP cells corresponding to *IMPACT* expression levels (Supplementary Fig. S7L; Supplementary Table S6). To evaluate *IMPACT* promoter methylation in human PAAD, we utilized three primary and five liver metastases. Compared with normal human pancreatic tissue, normal human liver tissue, and primary PAAD, liver metastases from human PAAD demonstrated significantly increased promoter methylation (Fig. 7K; Supplementary Table S6).

Finally, as expression of MHC-I and NK activation ligands on tumors correlates with immune cell infiltration and better patient survival, we examined the extent of immune cell abundance in the TME in relation to *IMPACT* expression. Intriguingly, *IMPACT* expression positively correlated with CD8 T-cell abundance and perforin activity as well as with other immune cell subsets both in PAAD and COAD (Fig. 7L and M; Supplementary Fig. S7M and S7N). However, this positive relationship is not strongly seen for NK cells, most likely because NK cells are short-lived and undergo degranulation releasing cytokines to activate other immune cells upon ligand–receptor engagement. Next, we stratified human PAAD tumors into *GCN1* high and *IMPACT* low using median expression and found that *GCN1*-high/*IMPACT*-low PAAD tumors were associated with lower survival probability compared with *GCN1*-low/*IMPACT*-high PAAD tumors (Fig. 7N). Moreover, *IMPACT* expression positively correlated with disease-free survival probability in both PAAD and COAD, and with OS in carcinomas with metastatic propensities (Fig. 7O and P; Supplementary Fig. S7O). Collectively, these data indicate that loss of IMPACT regulation on GCN1 signaling leads to immunometabolic plasticity that favors metastasis formation.

DISCUSSION

Disseminated tumor cells face numerous bottlenecks that impede survival immediately upon entry into target organs. First, these metastatic cells are exposed to the deleterious effects of oxidants from the incoming blood that sensitizes them to ferroptosis (99, 100). Second, tissue resident CD8 T cells that express tumor-specific TCRs can recognize antigens expressed on tumor cells to eliminate them (101). Third, tissue-resident NK cells with enhanced effector function predominate in nonlymphoid organs like the liver and lung, and can lyse tumor cells expressing stress ligands through engagement with their surface receptors (23, 31). Finally, metastatic cells that circumvent oxidative stress and escape immune surveillance must be proficient in assimilating nutrients to drive anabolic growth and produce biomass. This selective microenvironmental and immune pressure at distant organs sculpts aggressive tumor phenotypes with low immunogenicity but enhanced ability to withstand fatal redox alterations, and high competence to acquire nutrients in support of survival and growth.

Although tumor cells at the primary site utilize catabolic mechanisms like autophagy and macropinocytosis to acquire AAs for survival in a hypoxic, nutrient-poor microenvironment, outgrowth likely utilizes anabolic mechanisms that take precedence with abundant AAs (102–104). Rapidly proliferating tumor cells like those of pancreatic and colorectal cancer are highly addicted to glutamine and acquire it from plasma via various AA transporters to fuel the TCA. Targeting glutamine transporters (SLC1A5, SLC38A1, SLC38A2, SLC7A5, SLC7A7, SLC38A7, and SLC38A9) by glutamine-transport antagonists or specific synthetic mAbs has been shown to be effective in limiting *in vivo* and *in vitro* tumor cell growth (104–107). Likewise, the glutamine analogue sirpiglenastat (DRP-104), a prodrug version of 6-diazo-5-oxo-L-norleucine that broadly inhibits glutamine metabolism, has been shown to inhibit *in vivo* tumor growth in PAAD models and is currently in early-phase clinical trials (NCT04471415; refs. 108, 109). Glutamine also supports the biosynthesis of polyamines, which are small polycationic molecules required for tumor growth. Pancreatic adenocarcinoma cells upregulate the enzyme ornithine aminotransferase to drive polyamine biosynthesis, and inhibition of ornithine aminotransferase has been found to mitigate PAAD growth (110). More recently, PAAD cells have been shown to uptake alanine secreted by pancreatic stellate cells through SLC38A2 to support their *in vivo* growth, and inhibition of SLC38A2 has been suggested as a promising therapeutic target (111). Given the metabolic flexibility of tumor cells to utilize multiple transporters and pathways along with their propensity to crosstalk with nontumor cells in the TME in acquiring AAs, it is unlikely that targeting a single or a combination of AA transporters or AA biosynthetic enzymes will provide long-term clinical benefit.

Recent advances in augmenting immune responses to kill tumor cells have largely focused on enhancing T-cell function using immune checkpoint inhibitors. However, checkpoint interventions have shown clinical responses only in a limited pool of patients largely because most aggressively growing tumors are immunologically cold and lack significant T-cell number in the TME (112, 113). On the other hand, therapeutic strategies to activate NK cells by blocking NK cell inhibitory receptor NKG2A engagement with HLA-E using monalizumab also failed in clinical trials (ClinicalTrials.gov registration NCT04590963; refs. 14, 78, 114). Adoptive infusion of allogenic NK cells has also been largely unsuccessful in the treatment of solid tumors because of lack of their infiltration and target-cell recognition in the TME (115, 116). These data suggest that limited activation of $CD8^+$ T cells or NK cells in the TME through blockade of a single inhibitory receptor or *in vitro* activation of allogenic NK cells before infusion treatment is not enough to overcome the robust immunosuppressive signal exerted by the inhibitory receptors (LILRBs and KIRs) on NK cells and other monocytes through engagement with multiple tumor HLAs. There is an unmet need to identify mechanisms and pathways that not only tilt the balance in favor of NK activation but also enhance tumor immunogenicity to aid tumor cell recognition

in the TME, enabling NK and CD8+ T cell–dependent immunotherapies to be successful across a broad spectrum of patients with cancer.

At the molecular level, our findings suggest that the expression of the stress ligands including MHC-I polypeptide–related sequence A/B, the ULBP family of proteins (ULBP1-6), and B7-H6 (ligand for the NCR3) on the tumor cell surface upon GCN1 KD or IMPACT overexpression is a potent stimulation for NK cell recognition, activation, and tumor cell killing. To counteract this threat from NK cells, tumor cells upregulate the expression of MHC-I (both classical and nonclassical HLAs), which are ligands for the inhibitory receptors on NK cells such as the KIRs, LILRBs, and NKG2A (12, 13, 15). KIRs exhibit specific binding to the α2 domain of some classical MHC-I, whereas LILRs have broader specificity and bind to the more conserved α3 and β2 regions of all classical and nonclassical MHC-I molecules (except HLA-E), and CD94/NKG2A/C binds specifically to HLA-E (13, 114, 117, 118). Genetic ablation of *GCN1* or overexpression of IMPACT led to the activation of multiple mechanisms that support MHC-I expression, including the expression of TNFα and IFNγ, two major cytokines that are known regulators of APP molecules including classical MHC-I, TAP1, TAP2, and TPSN (68, 119, 120). The expression of TAP1, TAP2, and TPSN further stabilizes the surface expression of MHC-I to neutralize the threat posed by NK cells through engagement with their inhibitory receptors (121–123). In mouse, this threat is neutralized by the engagement of mouse MHC (H2-Db/H2-Kb) with the Ly49 family of inhibitory receptors expressed on NK cells and some T cells (12, 124). The upregulation of the negative regulators of the immune system PD-L1 and PD-L2 on tumor cells upon GCN1 KD or IMPACT overexpression is also a mechanism to overcome the threat posed by NK cell activation. However, due to the large array of NK ligands and proteoglycans/glycosaminoglycan that are altered by GCN1 KD or IMPACT overexpression, the combinatorial strength of signaling received from activating receptors outweighs the inhibitory signal generated from the engagement of tumor MHC-I with KIRs and LILRBs. As a result, IMPACT-OE cells are deemed stressed/altered and are eliminated by the cytolytic action of NK cells. Activation of NK cells releases IFNγ and TNFα to further engage the adaptive arm of the immune system, allowing CD8+ T cells to participate in tumor cell killing directly through secretion of granzyme/perforin independently of the TCR (125–128). We posit that innate-dependent activation of MHC-unrestricted cytotoxicity of adaptive immune cells can be leveraged in the treatment of immunologically "cold tumors" which are otherwise checkpoint resistant.

Taken together, our study indicates that targeting GCN1 signaling may be an optimal strategy to disrupt the immunometabolic plasticity of metastasis-initiating tumor cells. Blocking GCN1 function not only reduces the intracellular homeostatic balance of EAAs and NEAAs precipitously but leads to buildup of toxic ROS, causing metabolic crisis. Consequently, this metabolic stressor results in the expression of stress ligands on the tumor cell surface that are specifically recognized and marked by NK cells to engage and eliminate them. This molecular fail-safe mechanism prevents the undue propagation of defective/unhealthy cells to maintain tissue integrity and organismal homeostasis under normal physiologic conditions. However, cancer cells through upregulation of GCN1–HNRNPK signaling or loss of IMPACT expression (or both) leverage the ISR-dependent molecular program to activate AA uptake while simultaneously suppressing the innate immune response to maintain perpetual growth compromising tissue integrity. We propose that small molecules (IMPACT mimetics) able to disrupt GCN1–GCN2 and GCN1–HNRNPK signaling can be therapeutically exploited to curtail metabolic plasticity and augment tumor immunogenicity. Such mimetics or "immunogenicity augmenters" can stimulate host NK cells to delay/prevent metastatic growth either alone or synergistically with ICB both in adjuvant and neoadjuvant settings.

Although HNRNPK is involved in mRNA degradation which occurs in the cytosol, it is unclear how this function is executed considering that HNRNPK is predominantly localized in the nucleus in the pancreatic tumor cell lines. The involvement of other heterogeneous ribonucleoproteins in this process also cannot be ruled out as most heterogeneous ribonucleoproteins work in complexes. Although cytoplasmic mRNA decay is the dominant mechanism of mRNA turnover in eukaryotes, nuclear RNA degradation and recycling might be more ubiquitous than expected in aggressive cancer lines. The full mechanistic biology behind HNRNPK's role in mRNA turnover warrants further investigation. The conclusions derived in this work on the role and function of GCN1, IMPACT, and HNRNPK were based on mRNA expression. All commercially available IHC antibodies against GCN1, IMPACT, and HNRNPK were tested for staining of tumor sections and tissue microarrays. Unfortunately, tumor staining was found weak and nonspecific even at high dilutions upon thorough examination by an external pathologist. Henceforth, further IHC validation on the expression of these proteins in human tumors was not possible.

METHODS

Cell Lines and Plasmids

The mouse KPC-4964 cell line was a kind gift from Dr. Anil K Rustgi of Herbert Irving Comprehensive Cancer Center at Columbia University. The syngeneic mouse KPC177669 cell line and the human pancreatic KLM1 cell line were provided by Dr. Serguei Kozlov and Dr. Christine Campo Alewine, respectively, at the NCI. The breast cancer cell lines MCF-7, ZR751, MDAMB-231 and LM2 were obtained from the laboratory of late Prof. Filippo Giancotti. The 293T, HPNE, BXPC3, ASPC1, HPAFII, PANC1, SW1990, MIAPACA, PATU8988T and SU.86.86 cell lines were freshly obtained from commercial vendors (ATCC or DSMZ). All cell lines were *Mycoplasma*-tested by PCR and maintained in DMEM or DMEM/F12 supplemented with 10% FBS, 1× penicillin/streptomycin, and 2.5 μg/mL Plasmocin for eliminating and preventing *Mycoplasma*-related effects.

The CMV51p>ffluc2-mEmerald (EL) lentiviral plasmid was generated by subcloning three entry clones (*Cytomegalovirus* promoter, ffluc2, and mEmerald) into pDest-676, a neomycin-resistant lentiviral backbone, using Gateway MultiSite recombination. The reaction was transformed into Stbl3 *Escherichia coli* cells, and the correct clone was chosen based on supercoiled size and restriction digest pattern. The plasmid DNA was prepared for lentivirus production using the

Qiagen Plasmid Plus Maxi Kit. The KPCEL cell line was generated by transducing the KPC177669 cells with the mEmerald-luciferase (EL) lentiviral plasmid generated above and selecting transduced cells in neomycin for 1 week. The KPC-4964 cell line was transduced with a lentivirus containing an mCherry-luciferase cassette to produce a stable 4964 cell line expressing mCherry and luciferase. The resulting cell line was used for generating low and high liver metastatic cell lines by *in vivo* passaging in mice. The FLAG-GCN1 and FLAG-IMPACT expression plasmids used in GST pull-down assays were cloned in pcDNA3.1. The 3XFLAG-tagged mouse IMPACT sequence was subcloned in pLentiCMV-V5-luciferase (Addgene #21474) replacing the V5-luciferase cassette. The plasmids expressing V5-ATF4 (EX-OL00117-LX304), V5-IMPACT (EX-OL03588-LX304), and HNRNPK (EX-X0648-M98) were purchased from GeneCopoeia. The 3′-UTR sequences of immune genes were cloned downstream of the luciferase gene in the pmiR-GLO dual luciferase reporter vector and sequence-verified. All reagents and cell lines used in the study are listed in Supplementary Table S7.

Generation of Short Hairpin RNA KD, CRISPR KO, and cDNA Overexpression Cell Lines

For generating stable KD, KO, and overexpression cell lines, viral supernatants were generated by transfecting 293T cells with specific shRNAs, single-guide RNAs (sgRNA), and cDNA constructs along with packaging plasmids pMD2G and psPAX. pLKO.1 plasmids encoding shRNAs targeting mouse GCN1 (SH1-TRCN0000251695 and SH2-TRCN0000251694), human GCN1 (SH1-TRCN0000154822, SH2-TRCN0000155944, and SH3-TRCN0000155124), mouse HNRNPK (SH1-TRCN0000096825 and SH2-TRCN0000096827), and human XRN2 (SH1-TRCN0000049899 and SH2-TRCN0000293639) were obtained from MISSION Sigma. The human SMARTvector lentiviral control and HNRNPK shRNAs (#V3SH11252-230110420 and #V3SH11252-230819326) were obtained from Dharmacon. The sgRNA sequence for IMPACT KO was designed using the web-based program from Broad Institute (www.portals.broadinstitute.org/gppx/crispick/public). Briefly, annealed oligonucleotides carrying the sgRNA target sequence (exon 2 TTCAGAGTGAAGAAATCGAAGCAATGGCAG) were cloned into lentiCRISPRv2 (one vector system). The sgRNA control sequence (CACCGGCACTACCAGAGCTAACTCA) in lentiCRISPRv2 was obtained from Addgene (#125836).

Retroviral cDNA Screen

We constructed a high-complexity cDNA library (~2×10^6 independent clones) from mRNA isolated from the highly metastatic cell line 4964-HM. The mRNA was size-fractionated into three pools (>3, 1–3, and <1 Kb), and the respective cDNA libraries were cloned into a modified retroviral shuttle vector pEYK3.1 as previously described (25, 26). The retroviral libraries were independently transduced into the low metastatic 4964-POP cells (MOI = 1) and injected into the spleen of nude mice (0.3×10^6 cells/mice). Mice were monitored weekly to determine the growth of liver metastatic lesions using bioluminescence imaging. Macroscopic lesions at the end of 6 weeks were extirpated, minced, and digested with trypsin to isolate clonogenic tumor cells which were expanded in selective medium. Integrated proviral DNA was identified using genomic DNA isolation, amplification of proviral DNA with the vector-specific primer, and sequencing.

Metabolite Assay by LC/MS

GSH, acetyl-CoA, α-KG, and other reference compounds and chemicals were obtained from Sigma. The AA standard mixture and the isotopic internal standards (IS) were obtained from Cambridge Isotope Laboratories, Inc. The AAs, GSH, and the corresponding internal standard stock solutions were prepared in water. The calibration standard solutions were prepared by serial dilution of the stock solutions with water. The working IS solution (25 μmol/L) was prepared by diluting the IS stocks with water. Sodium carbonate (100 mmol/L) was prepared in water. Benzoyl chloride solution (1%, v/v) was prepared in acetonitrile. Cell pellets were extracted with 80% methanol in water supplemented with appropriate isotopic standards. All the extracted samples were centrifuged to obtain the supernatants for analysis. The metabolites were determined using LC/MS after chemical derivatization with benzoyl chloride as described by Wong and colleagues (129) with slight modification. In a 500-μL polypropylene tube, 10 μL of the supernatant (or standard solution), 10 μL of sodium carbonate, 10 μL of IS, and 20 μL of benzoyl chloride were mixed for several minutes. Twenty microliters of the reaction mixture was diluted with 20 μL of water, and the solution was transferred to polypropylene sample injection vials. Liquid chromatography was performed using a Shimadzu 20AC-XR system. Separation was achieved at 50°C with a 2.1 × 100 mm, 1.8-μm T3 column (Waters). Mobile phase A was 0.15% formic acid with 10 mmol/L ammonium formate in water, and mobile phase B was acetonitrile. The flow rate was 300 μL/minute, and the injection volume was 2 μL. The metabolites were separated with a gradient (0–0.2 minutes/2% B; 15 minutes/60% B; 15.1–16 minutes/95% B; 16.1–18 minutes/2% B). MS-MS was performed using a TSQ Quantiva Triple Quadrupole Mass Spectrometer (Thermo Fisher Scientific) operating in positive (selected reaction monitoring) SRM mode. The metabolites in the samples were determined using linear calibration curves with 1/x weighting generated using Thermo Fisher Scientific Xcalibur Quan Browser software. The calibration curves were constructed by plotting the peak area ratios versus standard concentrations. The peak area ratio was calculated by dividing the peak area of the metabolites by the peak area of the corresponding IS.

Isotope Uptake

Isotopes L-glutamine D5 (DNLM-1826) and L-leucine D10, 15N (DNLM-4643) were obtained from Cambridge Isotope laboratories, Inc. Cells were grown in the isotope-containing medium for 16 hours, washed in cold 1× PBS, and harvested in 80% methanol. Isotope uptake was quantitated using LC-MS.

RNA-seq Gene Expression Profiling and Pathway Analysis

KPC177669 (mouse) and KLM1 (human) pancreatic cancer cells expressing control shRNA (SCR) and GCN1-specific shRNAs (GCN1_SH1 and GCN1_Sh2) were cultured in DMEM and RNA isolated using RNeasy kit (Qiagen). Quality control assessment was done using Agilent TapeStation and Qubit assay. Paired-end RNA-seq profiles of duplicate samples for each condition were generated from Illumina NextSeq 2000 P2 run. Raw fastq files were trimmed using Cutadapt (v1.18) and aligned using STAR (v 2.7.0f) against GRCm38 (mm10). Duplicated reads were removed using Picard tools (v 2.17.11) and RSEM (v 1.3.0) to quantify gene counts. R (v 4.2.2) was used with package DESeq2 (v1.40.1) to determine differentially expressed genes (DEG; FDR < 0.05; $\log_2$ FC ± 1.3). Subsetting the resulting DEG lists was done based on the direction of the fold change to distinguish between up- and downregulated genes. For each subset, enriched pathways were identified with an overrepresentation analysis using Gene Ontology gene sets from the Molecular Signatures Database.

Single-Cell RNA-seq

Single-cell suspensions were prepared, and cell counts and viability measurement were taken for each suspension using a fluorescent cell counter with dual viability dyes composed of propidium iodide and acridine orange (LUNA-FL, Logos Biosystems). Sample concentrations were adjusted and loaded onto the 10× Genomics Chromium

platform using the 10× Genomics 3′ v4 Gene Expression Assay, targeting roughly 20,000 cells per sample. Preparation of single-cell gene expression libraries was performed according to vendor recommendations. Sequencing was performed on the Illumina NovaSeq X Plus instrument with 100-cycle kits using 10× recommended run parameters. Gene expression and feature barcode libraries for the two samples were multiplexed together at a ratio to achieve final target read sequencing depth. Base calling was performed using RTA4, and demultiplexing was performed using BCL Convert v4.1.23. Data were processed using the 10× Genomics Cell Ranger pipeline v9.0.0 (STAR 2.7.2a). Sequenced reads were aligned to a mouse reference sequence (refdata-gex-GRCm39-2024-A) provided by 10× Genomics to generate a single-cell GEX matrix. Downstream single-cell analysis and visualization were performed within the NIH Integrated Data Analysis Platform using R programs developed by a team of NCI bioinformaticians on the Foundry platform (Palantir Technologies). The single cell workflow on the NIH Integrated Data Analysis Platform is based on the Seurat workflow (v. 4.1.1; ref. 130).

Poly-C Content Measurement

A median poly-C content score was calculated for each gene to test for enrichment of cytosine-rich regions in 3′-UTR sequences. For a given 3′-UTR sequence for a given gene, a poly-C content score was calculated using a k-mer siding window approach. For a given position within the length of the 3′-UTR sequence, a counter was incremented when the k-mer matched the following sequence: "CCC." This counter was then divided by the number of the k-mer sequences encountered and multiplied by a scaling factor of 100. The median poly-C content score was calculated for a set of 3′-UTR sequences for a given gene.

Human Samples

Primary colorectal tumor and liver metastatic lesion were obtained from patients undergoing resection after receiving written informed consent at the NCI clinical center under protocol NCT13C0176 approved by the Institutional Review Board of the NIH.

Animal Studies

All animal protocols were reviewed and approved by the institutional animal care and use committees of Memorial Sloan Kettering Cancer Center and the NIH. All experiments were performed on 10- to 12-week-old male or female age- and sex-matched immunocompetent C57BL/6 mice or immunodeficient athymic nude mice or NSG-IL15 mice obtained from The Jackson laboratory. For liver outgrowth and colonization, 0.3 to 0.5 × 10^6 4964-POP, 4964-HOP, KPCEL, and KLM1 cells and their KD, KO, or overexpression derivatives in 50 μL of 1× PBS were injected intravenously through the spleen. For lung outgrowth and colonization, 0.3 to 0.5 × 10^6 cells in 100 μL of 1× PBS were intravenously injected through the tail vein of C57BL/6/RAG KO/Nude mice. Mice were humanely euthanized when they exhibited signs of morbidity and/or hind limb paralysis.

Splenic Injection and Liver Outgrowth Assay

Liver metastatic outgrowth and colonization were evaluated through intrasplenic injections. Briefly, the mouse is anesthetized, and an injection of 2 mg/kg of meloxicam and 0.5 mg/kg of buprenorphine is administered subcutaneously. Sterile eye lubricant is applied to both eyes to prevent corneal drying during surgery. When administering injections into the C57/BL6 mouse, the fur covering the abdominal wall is carefully removed by applying hair removal cream. The abdominal skin is then cleaned with a moist gauze pad to remove loose hair and sterilized with Betadine and 70% ethanol. A small volume of local anesthetic agent, such as bupivacaine (0.25%–0.5%), is injected into the tissue adjacent to the intended incision line. A 0.5- to 1-cm parasagittal incision is made in the skin of the left flank using sterile scissors, revealing the abdominal muscles. Sterile scissors are then used to make a 0.5- to 1-cm parasagittal incision through the abdominal musculature over the spleen. The spleen is exteriorized through the incision by gentle retraction with forceps and held in place using a sterile cotton–tipped applicator or placed on a sterile moist gauze pad. A total of 0.3 × 10^6 tumor cells in 100 μL of 1× PBS are injected into the splenic parenchyma under the splenic capsule using a 26-gauge needle. When the needle is withdrawn, gentle pressure is applied to the injection site using a sterile cotton swab or gauze for 3 to 5 minutes or until hemostasis is achieved. Three to five minutes after splenic injection when adequate hemostasis is achieved, the spleen is removed, and the splenic artery and vein are ligated using 6-0 suture. The abdomen is checked for bleeding. If bleeding is found, gentle pressure is applied using a cotton swab or sterile gauze until hemostasis is achieved. The muscle layer is closed using sterile absorbable suture (e.g., Vicryl) of the appropriate diameter in a simple interrupted pattern. Skin edges are opposed and closed with a monofilament absorbable suture (e.g., Monocryl) of the appropriate diameter in a subcuticular pattern. Immediately following surgery, when the mouse is under anesthesia, 100 μL of luciferin is given by retro-orbital injection to visualize tumor cells in the liver via IVIS imaging. Thereafter, mice were imaged weekly or at an experimental endpoint to visualize tumor outgrowth and colonization in the liver.

Tail-Vein Injection and Lung Outgrowth Assay

Mice were warmed by placing them under the heat lamp for approximately 5 to 10 minutes to dilate the tail veins. Warmed mice were restrained using a conventional restrainer (Braintree Scientific) to access the tail vein. Once the vein is located, 0.3 × 10^6 tumor cells in 100 μL of 1× PBS are then carefully and slowly injected using a 28G needle to avoid vascular overload or rupture. After removing the needle, pressure is applied over the injection site by gently holding a piece of gauze for approximately 30 seconds to prevent hematoma formation. The mouse is immediately anaesthetized, and 100 μL of luciferin is given by retro-orbital injection to visualize tumor cells in the lung via IVIS imaging. Thereafter, mice were imaged weekly or at an experimental endpoint to visualize tumor outgrowth and colonization in the lung.

IVIS Imaging and Metastatic Outgrowth Analysis

For analyzing metastatic outgrowth and colonization potential of tumor cells, recipient mice were anesthetized under isoflurane, injected with 100 μL (15 mg/mL) of luciferin retro-orbitally, and whole-body bioluminescent images acquired on IVIS Spectrum (PerkinElmer) at timepoints indicated. For liver colonization experiments in C57BL/6 mice, the abdominal fur is removed with hair removal cream prior to luciferin injection and imaging. The liver region was defined as the area between the sternum and middle of the abdominal area. For whole-organ (liver/lung) IVIS imaging at indicated experimental endpoints, mice were injected with 100 μL of luciferin retro-orbitally and humanely euthanized, following which their livers and lungs were excised and then imaged in IVIS Spectrum. Living Image software versions 4.5.2 and 4.7.2 was used to measure liver and lung colonization by drawing regions of interest (ROI) in the defined area and quantifying the bioluminescence signal of the ROIs in the physical calibration unit "radiance/photons." The Living Image software automatically normalizes sensitivity differences resulting from different exposure times without any user input required, when ROI values are expressed in a calibrated, physical unit.

Isolation of Liver and Lung Leukocytes

The liver/lung extirpated from a euthanized mouse was disrupted through a 0.75-μm cell strainer using the rubber side of a 3cc syringe into a 50-mL tube with 5 to 10 mL of RPMI media for each liver/lung.

The media containing cells from the liver/lung was centrifuged at 30 × *g* for 3 minutes to remove the hepatocytes and tumor cells, and the supernatant was transferred to a new tube. Following centrifugation at 1,500 rpm for 5 minutes, the cell pellet was resuspended in 32% Percoll solution and again centrifuged at 14°C, 2,000 rpm with no brake for 15 minutes. Red blood cells were removed by washing the cell pellet with 5 mL of ACK lysis buffer and centrifuging the samples at 1,500 rpm for 5 minutes. The cell pellet containing only immune cells was further washed 2× in complete RPMI media and used for surface and intracellular staining with specific antibodies.

Isolation of Human NK Cells

Human peripheral blood collected from healthy volunteers was acquired from NIH blood bank and was centrifuged at 2,000 rpm for 15 minutes (acceleration-1, deceleration-1) in SepMate tubes over Ficoll–Hypaque to obtain total leukocytes. Red blood cells were removed by washing the leukocytes with ACK lysis buffer, a single-cell suspension of the leukocyte buffy coat was washed with FACS buffer, and NK cells were isolated using NK cell microbead cocktail (Miltenyi Biotech) following the manufacturer's instructions on autoMACS Pro Separator. The cell number was determined by counting using a hemocytometer by trypan-blue exclusion staining. A total of 1×10^7 cells were adoptively transferred per NSG-hIL15 transgenic mouse harboring established subcutaneous tumors.

Patient Data Analysis

For differential gene expression analysis of *GCN1*, *ATF4*, and *IMPACT*, tumor stratification, and OS, we used the GSE71729 dataset obtained from the NCBI Gene Expression Omnibus (GEO; https://www.ncbi.nlm.nih.gov/geo/). The relevant samples used in our study from the dataset were 46 normal pancreas, 145 pancreatic tumor, 25 liver metastasis, 9 lymph node metastases, and 8 lung metastasis samples. Where applicable, DEGs were determined using R software (v 3.5.2) limma package (v 3.38.3). To categorize the expression of *GCN1*, *ATF4*, and *IMPACT* as high or low, we utilized the median/mean gene expression values of *GCN1*, *ATF4*, and *IMPACT* from the Moffitt dataset (GSE71729). These processes were performed in R software version 4.2.1 using the R packages "GEOquery," "tidyverse," "survival," "survAUC," and "ggpurbr." Kaplan–Meier OS plots (log-rank test) were generated using GraphPad Prism version 8. Generalized linear regression models were built to examine the relationship between *IMPACT* gene expression in the primary adenocarcinoma of the pancreas ($N = 145$) and the tumor subtypes (classical and basal) while controlling for the stroma subtype. *P* values were calculated using a generalized linear model controlling for the stroma subtype. Kaplan–Meier survival plots in other cancer subtypes were obtained from www.kmplot.com. All analyses were done at default parameters.

GST Pull-down Assay

Five micrograms of purified recombinant human GST-GCN2/GST-HNRNPK purchased from Creative BioMart was incubated with 50 µL of GSH agarose bead slurry (Thermo Fisher Scientific, #21516) for 1 hour at 4°C. After washing with RIPA lysis buffer, bead-bound GST-GCN2/GST-HNRNPK were incubated with 15 µg of either 293T control lysate or 293T lysate overexpressing FLAG-GCN1 or FLAG-IMPACT or both for 1 hour at 4°C. GST-GCN2/GST-HNRNPK bead-bound protein complexes were washed 3× in RIPA lysis buffer and eluted in 30 µL of 2× SDS gel loading dye after boiling the protein complexes at 95°C for 5 minutes. Binding complexes were resolved in 4% to 12% NuPAGE Bis-Tris gel (Invitrogen) with appropriate input controls and confirmed using immunoblotting with specific antibodies.

RT-qPCR Analysis

Total RNA was isolated using RNeasy kit (Qiagen), and first-strand cDNA was prepared using qScript cDNA synthesis kit (Quantabio) according to the manufacturer's protocol. qPCR was performed on the QuantStudio 6 Flex Real-Time system (Applied Biosystems). Predesigned gene-specific TaqMan primers were purchased from Thermo Fisher Scientific, and melting curve analysis was done at the end of the PCR cycle. All experiments were performed in triplicate and repeated at least three times. Primers used are listed in Supplementary Table S7.

Protein Lysis and Western Blotting

Protein lysates were harvested on ice by directly adding SDS lysis buffer supplemented with complete protease inhibitor cocktail (Roche, #11697498001) and quantified using Bio-Rad protein assay reagent. Following SDS-PAGE, proteins were transferred to nitrocellulose membranes (Thermo Scientific, #88018), blocked in TBS containing 5% BSA (Sigma, #A7906) for 30 minutes, and incubated with primary antibodies for 2 hours at room temperature. The membranes were washed with TBS containing 0.1% Tween followed by incubation with horseradish peroxidase–conjugated secondary antibodies for 1 hour at room temperature. The membranes were visualized using SuperSignal West Pico PLUS chemiluminescent substrate (Thermo Fisher Scientific, #34577). All antibodies used in Western blotting are listed in Supplementary Table S7.

Nuclear and Cytoplasmic Fractionation

Cells were scrapped and resuspended in cold PBS containing protease inhibitor cocktail (Roche, #11697498001). After centrifugation, the supernatant was discarded, and cell pellets were used for subcellular fractionation using the NE-PER Nuclear and Cytoplasmic Extraction Reagents (Thermo Fisher Scientific, #78835) following the manufacturer's instructions.

Co-immunoprecipitation and MS-MS

KPC cells grown to 75% confluency were washed 2× in ice-cold PBS containing protease inhibitor cocktail (Roche, #11697498001). The cells were then lysed in RIPA lysis buffer (20 mmol/L Tris-HCl, 300 mmol/L NaCl, and 5 mmol/L $MgCl_2$, pH 8.0) containing 1% sodium deoxycholate (Sigma) and complete protease inhibitor cocktail for 30 minutes on ice. Cell lysates were precleared with Protein A/G beads (Pierce, #20421) for 1 hour at 4°C. Five micrograms of antibody was added to the precleared lysate and incubated overnight with rotation at 4°C. Protein A/G beads were then added for immunoprecipitation and incubated for 3 hours at 4°C. Beads were centrifuged and washed 3 times with lysis buffer for 10 minutes each with rotation at 4°C. Protein complexes were then eluted from the beads by boiling in Laemmli buffer and separated by SDS-PAGE following which in-gel digestion was done overnight with trypsin. Extracted peptides were dried through lyophilization prior to MS-MS analysis on an Orbitrap Fusion Tribrid mass spectrometer (Thermo Fisher Scientific). Proteome Discoverer 2.3 (Thermo Fisher Scientific) was used to search the data against the UniProt murine database using SequestHT. The percolator node was used to score and rank peptide matches using a 1% FDR.

Nuclear Co-immunoprecipitation

Nuclear lysate from KPC cells was precleared with Protein A/G beads (Pierce, #20421) for 1 hour at 4°C. Fifteen micrograms of antibody was added to 2 mg of precleared nuclear lysate and incubated overnight with rotation at 4°C. Protein A/G beads were then added for immunoprecipitation and incubated for 3 hours at 4°C. Beads were centrifuged and washed 3 times with lysis buffer for 10 minutes

each with rotation at 4°C. Beads were then boiled in Laemmli sample buffer for 10 minutes at 95°C, and the supernatant was used for Western blotting. One percent of nuclear lysate was used as an input.

3-(4,5-Dimethylthiazol-2-yl)-2,5-diphenyltetrazolium bromide Assay

A total of 0.5×10^3 cells in a final volume of 200 μL culture medium were seeded in octuplicate in a 96-well plate and allowed to adhere overnight. Ten microliters (5 mg/mL) of 3-(4,5-dimethylthiazol-2-yl)-2,5-diphenyltetrazolium bromide (MilliporeSigma) was added directly into the media of each 96 well containing cells for proliferation assay and incubated at room temperature for 1 hour. Media was slowly and carefully removed and 50 μL of DMSO added per well and further incubated at 37°C for 30 minutes. 3-(4,5-Dimethylthiazol-2-yl)-2,5-diphenyltetrazolium bromide absorbance was read at 540 nm.

Luciferase Reporter Assay

293T cells were seeded in 12-well plates and allowed to adhere overnight. Cells were transfected with the pmiR-GLO dual-luciferase vector with or without the 3′-UTRs of immune genes together with the pcDNA-GFP-HNRNPK expression vector using Lipofectamine. The total amount of transfected DNA was equalized with the control pcDNA plasmid vector. Firefly luciferase activity was measured using the Dual-Glo Luciferase Assay System (Promega, #E2940) according to the manufacturer's protocol and values normalized to the internal control Renilla reporter.

Flow Cytometry

Leukocytes isolated from the lung or liver were washed in FACS buffer (1× PBS containing 10% heat-inactivated FBS with 0.05% sodium azide) followed by blocking with mouse TruStain FcX (BioLegend) for 5 minutes. Surface staining was done with specific antibodies indicated for 30 minutes at 4°C in FACS buffer. Thereafter, surface-stained cells were fixed and permeabilized with the Foxp3/Transcription Factor staining buffer Kit (Invitrogen, #00-5523-00) following the manufacturer's protocol. For intracellular staining, surface-stained immune cells were treated with 1× cell stimulation cocktail (Invitrogen, # 00-4970-93) and transporter inhibitor cocktail (Invitrogen, # 00-4980-93) for 3 hours at 37°C. Cells were then washed in FACS buffer and incubated with Ki-67/granzyme/cytokine antibodies overnight at 4°C. For tumor cell surface staining of MHC-I and NK ligands, cells transduced with indicated shRNAs after selection in specific antibiotic medium were blocked with species-specific TruStain FcX (BioLegend) for 5 minutes, followed by staining with specific antibody for 30 minutes at 4°C in FACS buffer. Intracellular staining of TNFα and IFNγ on tumor cells was done for 30 minutes at 4°C after treatment with protein transporter inhibitor cocktail (Invitrogen, # 00-4980-93) for 3 hours at 37°C. Finally, cells were washed 2× in FACS buffer and analyzed using the BD LSRFortessa X-20 cell analyzer. Antibodies used in surface staining of cells are listed in Supplementary Table S7.

CpG Island Methylation Detection Using MiSeq

The Purigen DNA extraction kit was used to isolate genomic DNA from normal pancreas and liver tissues. Invitrogen Methyl Primer Express V1.0 was used to design the bisulphite sequencing primers (BSP), with product size about 400 bp for MiSeq 2 × 250 bp sequencing. Then M13 tags were added to the primers for multiplexing and Illumina adapter addition in later steps. Two hundred nanograms of genomic DNA samples were converted using the NEBNext Enzymatic Methyl-seq Conversion Module, E7125L. The converted DNAs were eluted from purification beads with 20 μL elution buffer and diluted 1:5 with elution buffer (2 ng/μL). Clontech Ex Taq DNA polymerase was used for target amplification. Twenty-five microliters of PCRs contains 2.5 μL 10× buffer, 2 μL dNTP, 1 μL DMSO, 0.3 μL Ex Taq polymerase, 2 μL 500 pmol/L primer mix, 2 μL converted DNA, and 15.2 μL H_2O. PCR cycles were 95°C for 3 seconds, 94°C for 1 minute, 60°C for 1 minute, and 72°C for 1 minute for 35 cycles; final extension at 72°C for 5 minutes; and a 4°C hold. PCR products for the same sample were pooled (25 μL), cleaned with 0.8× SPRI (solid phase reversible immobilization) beads, and eluted with 25 μL H_2O. A measure of 10.5 μL of the PCR products was used in the 25 μL barcoding PCR (12.5 μL Invitrogen 2× Platinum Taq, 1 μL 10 μmol/L P5 primer, and 1 μL 10 μmol/L P7 primer). Barcoding PCR cycles were 95°C for 2 minutes, 95°C for 30 seconds, 55°C for 30 seconds, and 72°C for 3 minutes for three cycles; 95°C for 30 seconds and 72°C for 2 minutes for 10 cycles; final extension at 72°C for 5 minutes; and a 4°C hold. The barcoded PCR products (libraries) were pooled, cleaned with 0.8× SPRI beads, and eluted with low Tris-EDTA (TE) buffer. The Qubit HS DNA kit was used to quantitate the concentration, and TapeStation was used to determine the library size and concentration which was then converted to molar concentration. The libraries were sequenced on Illumina MiSeq with 250 + 8 + 8 + 250 cycles. Unmethylated Cs were converted to Ts, whereas methylated Cs remained as Cs in the sequence. The sequence reads were analyzed using Qiagen CLC Genomics Workbench 20 to quantify the methylation levels. The sequences of primers used are listed below:

M13 barcoding primers

P5: AATGATACGGCGACCACCGAGATCTACACAGCGATAGAC ACTCTTTCCCTACACGACGCTCTTCCGATCTAGCGATAG GTAAAACGACGGCCAGT;

P7: CAAGCAGAAGACGGCATACGAGATAACTCTCGGTGAC TGGAGTTCAGACGTGTGCTCTTCCGATCTAACTCTCG GGAAACAGCTATGACCATG;

hIMPACT_F1: GTAAAACGACGGCCAGTTGTGGATTGAGGTT TGAGTTT;

hIMPACT_R1: GGAAACAGCTATGACCATGCCCTCAACCATA TAACCCCTA;

mIMPACT_F: GTAAAACGACGGCCAGTAGGTTTTGTTGTATT GTTATATGAGTAGG;

mIMPACT_R: GGAAACAGCTATGACCATGCCCATATAACAACT CAACCAAAC.

Statistical Analysis

GraphPad Prism version 8.4.3 and Microsoft Excel were used for statistical analyses and graphical representation. Data are presented as mean ± SD. A two-tailed Student *t* test and two-way ANOVA were performed for comparison between groups. *P* values by Student *t* test and two-way ANOVA are ns, $P \geq 0.05$; *, $P < 0.05$; **, $P < 0.01$; ***, $P < 0.001$; ****, $P < 0.0001$.

Data Availability

All materials and data supporting the findings of this study are available from the corresponding authors upon reasonable request. RNA-seq data generated in this study from GCN1 KD mouse KPC177669 cells and human pancreatic KLM1 cells are available at GEO database GSE303691 and GSE303622, respectively. The single-cell immune transcriptomics data generated in this study from mouse KPC177669 control and IMPACT-OE cells can be found at GEO database GSE299485. Previously published RNA-seq and single-cell transcriptomics data reanalyzed in this study were obtained from GEO database GSE71729 and GSE154778, respectively.

Authors' Disclosures

M.M. Wach reports a patent for WO2021183527A1 issued. P.K. Singh reports grants from NCI, NIH, during the conduct of the study. J.C. Yang reports other support from Iovance outside the submitted

work, as well as a patent for T Cell Receptors pending and issued. C.A. Lyssiotis reports a patent for Targeting the Glutamine to Pyruvate Pathway for Treatment of Oncogenic Kras-Associated Cancer issued and a patent for Methods for Diagnosing and Treating Oncogenic Kras-Associated Cancer issued. M.B. Yaffe reports grants from NIH and MIT Center for Precision Cancer Medicine during the conduct of the study. No disclosures were reported by the other authors.

Authors' Contributions

S. Sinha: Conceptualization, data curation, formal analysis, supervision, validation, investigation, visualization, methodology, writing–original draft, project administration, writing–review and editing. **A.K. Panda:** Formal analysis, investigation, methodology. **R. Xavier das Neves:** Software, formal analysis. **Z.C. Nwosu:** Software, formal analysis. **K. Xu:** Software, formal analysis. **E. van Beek:** Investigation, methodology. **P.P. Desai:** Data curation, formal analysis, methodology. **S. Sindiri:** Software, formal analysis. **S. Chempati:** Software, formal analysis, methodology. **K. Remmert:** Software, formal analysis. **B. Gasmi:** Formal analysis, validation, methodology. **L. Bojmar:** Resources. **C. Zambirinis:** Resources. **A.J. Rossi:** Methodology. **R.I. Ayabe:** Methodology. **M.M. Wach:** Methodology. **J.D. McDonald:** Methodology. **S.M. Ruff:** Methodology. **E.A. Verbus:** Methodology. **A. Saif:** Methodology. **A.V. Eade:** Methodology. **C.M. Larrain:** Methodology. **L.R. Friedman:** Methodology. **S. Gupta:** Methodology. **A. Ranjan:** Formal analysis, methodology. **M.E. Teke:** Methodology. **T.M. Khan:** Methodology. **T.D. Prickett:** Methodology. **A.L. Sarvestani:** Methodology. **C.E. Ryan:** Methodology. **J.T. Lambdin:** Methodology. **K. Luberice:** Methodology. **S.N. Gregory:** Methodology. **S.C. Lux:** Methodology. **H. Hong:** Methodology. **A.J. Luna:** Software. **I.A. Alexander:** Formal analysis. **S.R. Akmal:** Formal analysis. **S.U. Rehman:** Formal analysis. **A. Rainey:** Formal analysis. **T.D. Prickett:** Resources. **V.N. Koparde:** Data curation, formal analysis, visualization. **S. Sevilla:** Data curation, software, formal analysis. **S.A. Kuhn:** Data curation, software, formal analysis. **K. Chan:** Resources, data curation, formal analysis, methodology. **Z. Sun:** Formal analysis, methodology. **N. Bubunenko:** Formal analysis. **E. Li:** Formal analysis. **C. Hannah:** Resources. **G. Gaga:** Resources, formal analysis, methodology. **T. Andresson:** Resources, data curation. **M.C. Cam:** Data curation, software, formal analysis. **X. Wu:** Data curation, software, formal analysis. **L.M. Jenkins:** Resources, data curation, formal analysis. **A.M. Blakely:** Resources. **J.L. Davis:** Resources. **G. Trinchieri:** Resources, software, formal analysis. **P.K. Singh:** Resources. **J.C. Yang:** Resources, validation. **M. Pasca di Magliano:** Data curation, formal analysis. **C.A. Lyssiotis:** Resources, data curation, formal analysis. **M.B. Yaffe:** Resources, software, formal analysis. **E.M. Shevach:** Resources, formal analysis, supervision. **J.M. Hernandez:** Resources, supervision, funding acquisition, project administration, writing–review and editing.

Acknowledgments

We would like to express our deepest gratitude to late Prof. Filippo Giancotti whose guidance was instrumental in laying the foundation for this research work. We are saddened by his loss and remain thankful for his invaluable contribution. We thank Dr. Anil K. Rustgi (Herbert Irving Comprehensive Cancer Center at Columbia University, New York), Dr. Serguei Kozlov (NCI/NIH, Frederick, Maryland), and Dr. Christine Campo Alewine (NCI/NIH, Bethesda, Maryland) for providing the KPC 4964, the KPC177669, and the human KLM1 pancreatic cell lines, respectively. We are grateful to Dr. Steven A. Rosenberg (NCI/NIH, Bethesda, Maryland) for providing genomic DNAs from liver metastatic lesions of patients with pancreatic cancer. We would also like to thank P.K. Singh for providing pancreatic cancer tissue microarrays. We thank the staff of the Flow Cytometry, Animal Housing, Protein and Nucleic Acid Production, and Genomics core facilities of the Center for Cancer Research, NCI/NIH, for their help with experiments. We also thank the computational resources of the NIH HPC Biowulf cluster (http://hpc.nih.gov) for help with bioinformatics analysis. We thank Emily Smith and Yuri Lin for their material support and manuscript edits. We thank Drs. Glenn Merlino, Lalage M. Wakefield, Kent W. Hunter, and David Lyden for their suggestions and time in reviewing the manuscript. K. Chan, T. Andresson, Z. Sun, N. Bubunenko, and X. Wu were supported by the NCI under contract number 75N91019D00024. Support from the Center for Cancer Research Single Cell Analysis Facility was funded by Frederick National Laboratory for Cancer Research (FNLCR) contract number 75N91019D00024.

Note

Supplementary data for this article are available at Cancer Discovery Online (http://cancerdiscovery.aacrjournals.org/).

Received July 23, 2024; revised May 21, 2025; accepted July 28, 2025; posted first July 31, 2025.

REFERENCES

1. Pandit S, Samant H, Kohli K, Shokouh-Amiri HM, Wellman G, Zibari GB. Incidental liver metastasis in pancreatic adenocarcinoma. J Surg Case Rep 2019;2019:rjz084.
2. Makohon-Moore AP, Zhang M, Reiter JG, Bozic I, Allen B, Kundu D, et al. Limited heterogeneity of known driver gene mutations among the metastases of individual patients with pancreatic cancer. Nat Genet 2017;49:358–66.
3. Schild T, Low V, Blenis J, Gomes AP. Unique metabolic adaptations dictate distal organ-specific metastatic colonization. Cancer Cell 2018;33:347–54.
4. Obenauf AC, Massagué J. Surviving at a distance: organ-specific metastasis. Trends Cancer 2015;1:76–91.
5. Massagué J, Ganesh K. Metastasis-initiating cells and ecosystems. Cancer Discov 2021;11:971–94.
6. Zambirinis CP, Midya A, Chakraborty J, Chou JF, Zheng J, McIntyre CA, et al. Recurrence after resection of pancreatic cancer: can radiomics predict patients at greatest risk of liver metastasis? Ann Surg Oncol 2022;29:4962–74.
7. Li X, Ramadori P, Pfister D, Seehawer M, Zender L, Heikenwalder M. The immunological and metabolic landscape in primary and metastatic liver cancer. Nat Rev Cancer 2021;21:541–57.
8. Peng H, Wisse E, Tian Z. Liver natural killer cells: subsets and roles in liver immunity. Cell Mol Immunol 2016;13:328–36.
9. Bojmar L, Zambirinis CP, Hernandez JM, Chakraborty J, Shaashua L, Kim J, et al. Multi-parametric atlas of the pre-metastatic liver for prediction of metastatic outcome in early-stage pancreatic cancer. Nat Med 2024;30:2170–80.
10. Cózar B, Greppi M, Carpentier S, Narni-Mancinelli E, Chiossone L, Vivier E. Tumor-infiltrating natural killer cells. Cancer Discov 2021;11:34–44.
11. Huntington ND, Cursons J, Rautela J. The cancer-natural killer cell immunity cycle. Nat Rev Cancer 2020;20:437–54.
12. Anfossi N, André P, Guia S, Falk CS, Roetynck S, Stewart CA, et al. Human NK cell education by inhibitory receptors for MHC class I. Immunity 2006;25:331–42.
13. Sim MJW, Brennan P, Wahl KL, Lu J, Rajagopalan S, Sun PD, et al. Innate receptors with high specificity for HLA class I-peptide complexes. Sci Immunol 2023;8:eadh1781.
14. André P, Denis C, Soulas C, Bourbon-Caillet C, Lopez J, Arnoux T, et al. Anti-NKG2A mAb is a checkpoint inhibitor that promotes anti-tumor immunity by unleashing both T and NK cells. Cell 2018;175:1731–43.e13.
15. Barkal AA, Weiskopf K, Kao KS, Gordon SR, Rosental B, Yiu YY, et al. Engagement of MHC class I by the inhibitory receptor LILRB1 suppresses macrophages and is a target of cancer immunotherapy. Nat Immunol 2018;19:76–84.

16. Zhao J, Zhong S, Niu X, Jiang J, Zhang R, Li Q. The MHC class I-LILRB1 signalling axis as a promising target in cancer therapy. Scand J Immunol 2019;90:e12804.
17. Fuertes MB, Girart MV, Molinero LL, Domaica CI, Rossi LE, Barrio MM, et al. Intracellular retention of the NKG2D ligand MHC class I chain-related gene A in human melanomas confers immune privilege and prevents NK cell-mediated cytotoxicity. J Immunol 2008;180:4606–14.
18. Clayton A, Mitchell JP, Court J, Linnane S, Mason MD, Tabi Z. Human tumor-derived exosomes down-modulate NKG2D expression. J Immunol 2008;180:7249–58.
19. Kaiser BK, Yim D, Chow IT, Gonzalez S, Dai Z, Mann HH, et al. Disulphide-isomerase-enabled shedding of tumour-associated NKG2D ligands. Nature 2007;447:482–6.
20. Ponath V, Hoffmann N, Bergmann L, Mäder C, Alashkar Alhamwe B, Preußer C, et al. Secreted ligands of the NK cell receptor NKp30: B7-H6 is in contrast to BAG6 only marginally released via extracellular vesicles. Int J Mol Sci 2021;22:2189.
21. Carosella ED, Gregori S, Tronik-Le Roux D. HLA-G/LILRBs: a cancer immunotherapy challenge. Trends Cancer 2021;7:389–92.
22. Sharma N, Atolagbe OT, Ge Z, Allison JP. LILRB4 suppresses immunity in solid tumors and is a potential target for immunotherapy. J Exp Med 2021;218:e20201811.
23. Mikulak J, Bruni E, Oriolo F, Di Vito C, Mavilio D. Hepatic natural killer cells: organ-specific sentinels of liver immune homeostasis and physiopathology. Front Immunol 2019;10:946.
24. Gonzalez-Gugel E, Saxena M, Bhardwaj N. Modulation of innate immunity in the tumor microenvironment. Cancer Immunol Immunother 2016;65:1261–8.
25. Gao H, Chakraborty G, Lee-Lim AP, Mavrakis KJ, Wendel HG, Giancotti FG. Forward genetic screens in mice uncover mediators and suppressors of metastatic reactivation. Proc Natl Acad Sci U S A 2014;111:16532–7.
26. Gao H, Chakraborty G, Zhang Z, Akalay I, Gadiya M, Gao Y, et al. Multi-organ site metastatic reactivation mediated by non-canonical discoidin domain receptor 1 signaling. Cell 2016;166:47–62.
27. De Santis MC, Bockorny B, Hirsch E, Cappello P, Martini M. Exploiting pancreatic cancer metabolism: challenges and opportunities. Trends Mol Med 2024;30:592–604.
28. Takano S, Reichert M, Bakir B, Das KK, Nishida T, Miyazaki M, et al. Prrx1 isoform switching regulates pancreatic cancer invasion and metastatic colonization. Genes Dev 2016;30:233–47.
29. Hingorani SR, Wang L, Multani AS, Combs C, Deramaudt TB, Hruban RH, et al. Trp53R172H and KrasG12D cooperate to promote chromosomal instability and widely metastatic pancreatic ductal adenocarcinoma in mice. Cancer Cell 2005;7:469–83.
30. Yamazaki H, Kasai S, Mimura J, Ye P, Inose-Maruyama A, Tanji K, et al. Ribosome binding protein GCN1 regulates the cell cycle and cell proliferation and is essential for the embryonic development of mice. PLoS Genet 2020;16:e1008693.
31. Cong J, Wei H. Natural killer cells in the lungs. Front Immunol 2019;10:1416.
32. Marton MJ, Crouch D, Hinnebusch AG. GCN1, a translational activator of GCN4 in Saccharomyces cerevisiae, is required for phosphorylation of eukaryotic translation initiation factor 2 by protein kinase GCN2. Mol Cell Biol 1993;13:3541–56.
33. Sattlegger E, Hinnebusch AG. Polyribosome binding by GCN1 is required for full activation of eukaryotic translation initiation factor 2{alpha} kinase GCN2 during amino acid starvation. J Biol Chem 2005;280:16514–21.
34. Costa-Mattioli M, Walter P. The integrated stress response: from mechanism to disease. Science 2020;368:eaat5314.
35. Harding HP, Zhang Y, Zeng H, Novoa I, Lu PD, Calfon M, et al. An integrated stress response regulates amino acid metabolism and resistance to oxidative stress. Mol Cell 2003;11:619–33.
36. Ye J, Kumanova M, Hart LS, Sloane K, Zhang H, De Panis DN, et al. The GCN2-ATF4 pathway is critical for tumour cell survival and proliferation in response to nutrient deprivation. EMBO J 2010;29:2082–96.
37. Sullivan MR, Mattaini KR, Dennstedt EA, Nguyen AA, Sivanand S, Reilly MF, et al. Increased serine synthesis provides an advantage for tumors arising in tissues where serine levels are limiting. Cell Metab 2019;29:1410–21.e4.
38. Ye J, Fan J, Venneti S, Wan YW, Pawel BR, Zhang J, et al. Serine catabolism regulates mitochondrial redox control during hypoxia. Cancer Discov 2014;4:1406–17.
39. Zhu J, Berisa M, Schwörer S, Qin W, Cross JR, Thompson CB. Transsulfuration activity can support cell growth upon extracellular cysteine limitation. Cell Metab 2019;30:865–76.e5.
40. Sivanand S, Vander Heiden MG. Emerging roles for branched-chain amino acid metabolism in cancer. Cancer Cell 2020;37:147–56.
41. Kim M, Gwak J, Hwang S, Yang S, Jeong SM. Mitochondrial GPT2 plays a pivotal role in metabolic adaptation to the perturbation of mitochondrial glutamine metabolism. Oncogene 2019;38:4729–38.
42. Butler M, van der Meer LT, van Leeuwen FN. Amino acid depletion therapies: starving cancer cells to death. Trends Endocrinol Metab 2021;32:367–81.
43. Badgley MA, Kremer DM, Maurer HC, DelGiorno KE, Lee HJ, Purohit V, et al. Cysteine depletion induces pancreatic tumor ferroptosis in mice. Science 2020;368:85–9.
44. Xia J, Zhang J, Wu X, Du W, Zhu Y, Liu X, et al. Blocking glycine utilization inhibits multiple myeloma progression by disrupting glutathione balance. Nat Commun 2022;13:4007.
45. Mazari AMA, Zhang L, Ye ZW, Zhang J, Tew KD, Townsend DM. The multifaceted role of glutathione S-transferases in Health and disease. Biomolecules 2023;13:688.
46. Hayes JD, Dinkova-Kostova AT, Tew KD. Oxidative stress in cancer. Cancer Cell 2020;38:167–97.
47. Lee D, Xu IM, Chiu DK, Lai RK, Tse AP, Lan Li L, et al. Folate cycle enzyme MTHFD1L confers metabolic advantages in hepatocellular carcinoma. J Clin Invest 2017;127:1856–72.
48. Zarou MM, Vazquez A, Vignir Helgason G. Folate metabolism: a re-emerging therapeutic target in haematological cancers. Leukemia 2021;35:1539–51.
49. Raghunath A, Sundarraj K, Nagarajan R, Arfuso F, Bian J, Kumar AP, et al. Antioxidant response elements: discovery, classes, regulation and potential applications. Redox Biol 2018;17:297–314.
50. Bhutia YD, Babu E, Ramachandran S, Ganapathy V. Amino acid transporters in cancer and their relevance to "glutamine addiction": novel targets for the design of a new class of anticancer drugs. Cancer Res 2015;75:1782–8.
51. Kahya U, Köseer AS, Dubrovska A. Amino acid transporters on the guard of cell genome and epigenome. Cancers (Basel) 2021;13:125.
52. Abla H, Sollazzo M, Gasparre G, Iommarini L, Porcelli AM. The multifaceted contribution of α-ketoglutarate to tumor progression: an opportunity to exploit? Semin Cell Dev Biol 2020;98:26–33.
53. Carrer A, Trefely S, Zhao S, Campbell SL, Norgard RJ, Schultz KC, et al. Acetyl-CoA metabolism supports multistep pancreatic tumorigenesis. Cancer Discov 2019;9:416–35.
54. Sattlegger E, Swanson MJ, Ashcraft EA, Jennings JL, Fekete RA, Link AJ, et al. YIH1 is an actin-binding protein that inhibits protein kinase GCN2 and impairs general amino acid control when overexpressed. J Biol Chem 2004;279:29952–62.
55. Pereira CM, Sattlegger E, Jiang HY, Longo BM, Jaqueta CB, Hinnebusch AG, et al. IMPACT, a protein preferentially expressed in the mouse brain, binds GCN1 and inhibits GCN2 activation. J Biol Chem 2005;280:28316–23.
56. Cambiaghi TD, Pereira CM, Shanmugam R, Bolech M, Wek RC, Sattlegger E, et al. Evolutionarily conserved IMPACT impairs various stress responses that require GCN1 for activating the eIF2 kinase GCN2. Biochem Biophys Res Commun 2014;443:592–7.
57. Friedrich D, Marintchev A, Arthanari H. The metaphorical swiss army knife: the multitude and diverse roles of HEAT domains in eukaryotic translation initiation. Nucleic Acids Res 2022;50:5424–42.
58. Minn AJ, Gupta GP, Siegel PM, Bos PD, Shu W, Giri DD, et al. Genes that mediate breast cancer metastasis to lung. Nature 2005;436:518–24.

59. Furnish M, Boulton DP, Genther V, Grofova D, Ellinwood ML, Romero L, et al. MIRO2 regulates prostate cancer cell growth via GCN1-dependent stress signaling. Mol Cancer Res 2022;20:607–21.
60. González S, López-Soto A, Suarez-Alvarez B, López-Vázquez A, López-Larrea C. NKG2D ligands: key targets of the immune response. Trends Immunol 2008;29:397–403.
61. Koch J, Steinle A, Watzl C, Mandelboim O. Activating natural cytotoxicity receptors of natural killer cells in cancer and infection. Trends Immunol 2013;34:182–91.
62. Stern N, Markel G, Arnon TI, Gruda R, Wong H, Gray-Owen SD, et al. Carcinoembryonic antigen (CEA) inhibits NK killing via interaction with CEA-related cell adhesion molecule 1. J Immunol 2005; 174:6692–701.
63. Shi H, Tsang Y, Yang Y. Identification of CEACAM5 as a stemness-related inhibitory immune checkpoint in pancreatic cancer. BMC Cancer 2022;22:1291.
64. Pandey R, Zhou M, Islam S, Chen B, Barker NK, Langlais P, et al. Carcinoembryonic antigen cell adhesion molecule 6 (CEACAM6) in Pancreatic Ductal Adenocarcinoma (PDA): an integrative analysis of a novel therapeutic target. Sci Rep 2019;9:18347.
65. Wang J, Lu Q, Chen X, Aifantis I. Targeting MHC-I inhibitory pathways for cancer immunotherapy. Trends Immunol 2024;45:177–87.
66. Ohaegbulam KC, Assal A, Lazar-Molnar E, Yao Y, Zang X. Human cancer immunotherapy with antibodies to the PD-1 and PD-L1 pathway. Trends Mol Med 2015;21:24–33.
67. Garcia-Diaz A, Shin DS, Moreno BH, Saco J, Escuin-Ordinas H, Rodriguez GA, et al. Interferon receptor signaling pathways regulating PD-L1 and PD-L2 expression. Cell Rep 2017;19:1189–201.
68. Kearney CJ, Vervoort SJ, Hogg SJ, Ramsbottom KM, Freeman AJ, Lalaoui N, et al. Tumor immune evasion arises through loss of TNF sensitivity. Sci Immunol 2018;3:eaar3451.
69. Gao J, Shi LZ, Zhao H, Chen J, Xiong L, He Q, et al. Loss of IFN-γ pathway genes in tumor cells as a mechanism of resistance to anti-CTLA-4 therapy. Cell 2016;167:397–404.e9.
70. Yoshihama S, Vijayan S, Sidiq T, Kobayashi KS. NLRC5/CITA: a key player in cancer immune surveillance. Trends Cancer 2017;3:28–38.
71. Lopes N, Vivier E, Narni-Mancinelli E. Natural killer cells and type 1 innate lymphoid cells in cancer. Semin Immunol 2023;66:101709.
72. Ducimetière L, Lucchiari G, Litscher G, Nater M, Heeb L, Nuñez NG, et al. Conventional NK cells and tissue-resident ILC1s join forces to control liver metastasis. Proc Natl Acad Sci U S A 2021;118:e2026271118.
73. Curio S, Belz GT. The unique role of innate lymphoid cells in cancer and the hepatic microenvironment. Cell Mol Immunol 2022;19:1012–29.
74. Gotthardt D, Putz EM, Grundschober E, Prchal-Murphy M, Straka E, Kudweis P, et al. STAT5 is a key regulator in NK cells and acts as a molecular switch from tumor surveillance to tumor promotion. Cancer Discov 2016;6:414–29.
75. Moriggl R, Topham DJ, Teglund S, Sexl V, McKay C, Wang D, et al. Stat5 is required for IL-2-induced cell cycle progression of peripheral T cells. Immunity 1999;10:249–59.
76. Daniels MA, Luera D, Teixeiro E. NFκB signaling in T cell memory. Front Immunol 2023;14:1129191.
77. Hsu J, Hodgins JJ, Marathe M, Nicolai CJ, Bourgeois-Daigneault MC, Trevino TN, et al. Contribution of NK cells to immunotherapy mediated by PD-1/PD-L1 blockade. J Clin Invest 2018;128:4654–68.
78. Borst L, van der Burg SH, van Hall T. The NKG2A-HLA-E Axis as a novel checkpoint in the tumor microenvironment. Clin Cancer Res 2020;26:5549–56.
79. Aryee KE, Burzenski LM, Yao LC, Keck JG, Greiner DL, Shultz LD, et al. Enhanced development of functional human NK cells in NOD-scid-IL2rg(null) mice expressing human IL15. FASEB J 2022;36:e22476.
80. Guerra N, Tan YX, Joncker NT, Choy A, Gallardo F, Xiong N, et al. NKG2D-deficient mice are defective in tumor surveillance in models of spontaneous malignancy. Immunity 2008;28:571–80.
81. Falcomatà C, Bärthel S, Schneider G, Rad R, Schmidt-Supprian M, Saur D. Context-specific determinants of the immunosuppressive tumor microenvironment in pancreatic cancer. Cancer Discov 2023;13:278–97.
82. Li J, Byrne KT, Yan F, Yamazoe T, Chen Z, Baslan T, et al. Tumor cell-intrinsic factors underlie heterogeneity of immune cell infiltration and response to immunotherapy. Immunity 2018;49:178–93.e7.
83. Lammens K, Bemeleit DJ, Möckel C, Clausing E, Schele A, Hartung S, et al. The Mre11:Rad50 structure shows an ATP-dependent molecular clamp in DNA double-strand break repair. Cell 2011;145:54–66.
84. Chen Y, Zeng Y, Xiao Z, Chen S, Li Y, Zou J, et al. Role of heterogeneous nuclear ribonucleoprotein K in tumor development. J Cell Biochem 2019;120:14296–305.
85. Zhou W, Jie Q, Pan T, Shi J, Jiang T, Zhang Y, et al. Single-cell RNA binding protein regulatory network analyses reveal oncogenic HNRNPK-MYC signalling pathway in cancer. Commun Biol 2023;6:82.
86. Escobar-Hoyos LF, Penson A, Kannan R, Cho H, Pan CH, Singh RK, et al. Altered RNA splicing by mutant p53 activates oncogenic RAS signaling in pancreatic cancer. Cancer Cell 2020;38:198–211.e8.
87. Li Y, Wang H, Wan J, Ma Q, Qi Y, Gu Z. The hnRNPK/A1/R/U complex regulates gene transcription and translation and is a favorable prognostic biomarker for human colorectal adenocarcinoma. Front Oncol 2022;12:845931.
88. Nguyen Ba AN, Pogoutse A, Provart N, Moses AM. NLStradamus: a simple Hidden Markov Model for nuclear localization signal prediction. BMC Bioinformatics 2009;10:202.
89. Li J, Chen Y, Xu X, Jones J, Tiwari M, Ling J, et al. HNRNPK maintains epidermal progenitor function through transcription of proliferation genes and degrading differentiation promoting mRNAs. Nat Commun 2019;10:4198.
90. Yano M, Okano HJ, Okano H. Involvement of Hu and heterogeneous nuclear ribonucleoprotein K in neuronal differentiation through p21 mRNA post-transcriptional regulation. J Biol Chem 2005;280:12690–9.
91. Mikula M, Bomsztyk K, Goryca K, Chojnowski K, Ostrowski J. Heterogeneous nuclear ribonucleoprotein (HnRNP) K genome-wide binding survey reveals its role in regulating 3′-end RNA processing and transcription termination at the early growth response 1 (EGR1) gene through XRN2 exonuclease. J Biol Chem 2013;288:24788–98.
92. Thisted T, Lyakhov DL, Liebhaber SA. Optimized RNA targets of two closely related triple KH domain proteins, heterogeneous nuclear ribonucleoprotein K and alphaCP-2KL, suggest distinct modes of RNA recognition. J Biol Chem 2001;276:17484–96.
93. Krismer K, Bird MA, Varmeh S, Handly ED, Gattinger A, Bernwinkler T, et al. Transite: a computational motif-based analysis platform that identifies RNA-binding proteins modulating changes in gene expression. Cell Rep 2020;32:108064.
94. Lin W, Noel P, Borazanci EH, Lee J, Amini A, Han IW, et al. Single-cell transcriptome analysis of tumor and stromal compartments of pancreatic ductal adenocarcinoma primary tumors and metastatic lesions. Genome Med 2020;12:80.
95. Moffitt RA, Marayati R, Flate EL, Volmar KE, Loeza SG, Hoadley KA, et al. Virtual microdissection identifies distinct tumor- and stroma-specific subtypes of pancreatic ductal adenocarcinoma. Nat Genet 2015;47:1168–78.
96. O'Kane GM, Grünwald BT, Jang GH, Masoomian M, Picardo S, Grant RC, et al. GATA6 expression distinguishes classical and basal-like subtypes in advanced pancreatic cancer. Clin Cancer Res 2020; 26:4901–10.
97. Decker K, Goldman DC, Grasch CL, Sussel L. Gata6 is an important regulator of mouse pancreas development. Dev Biol 2006;298:415–29.
98. Eyres M, Lanfredini S, Xu H, Burns A, Blake A, Willenbrock F, et al. TET2 drives 5hmc marking of GATA6 and epigenetically defines pancreatic ductal adenocarcinoma transcriptional subtypes. Gastroenterology 2021;161:653–68.e16.
99. Tasdogan A, Ubellacker JM, Morrison SJ. Redox regulation in cancer cells during metastasis. Cancer Discov 2021;11:2682–92.
100. Piskounova E, Agathocleous M, Murphy MM, Hu Z, Huddlestun SE, Zhao Z, et al. Oxidative stress inhibits distant metastasis by human melanoma cells. Nature 2015;527:186–91.
101. Frank ML, Lu K, Erdogan C, Han Y, Hu J, Wang T, et al. T-cell receptor repertoire sequencing in the era of cancer immunotherapy. Clin Cancer Res 2023;29:994–1008.

102. Yang A, Rajeshkumar NV, Wang X, Yabuuchi S, Alexander BM, Chu GC, et al. Autophagy is critical for pancreatic tumor growth and progression in tumors with p53 alterations. Cancer Discov 2014;4:905–13.
103. Commisso C, Davidson SM, Soydaner-Azeloglu RG, Parker SJ, Kamphorst JJ, Hackett S, et al. Macropinocytosis of protein is an amino acid supply route in Ras-transformed cells. Nature 2013;497:633–7.
104. Palm W, Araki J, King B, DeMatteo RG, Thompson CB. Critical role for PI3-kinase in regulating the use of proteins as an amino acid source. Proc Natl Acad Sci U S A 2017;114:E8628–e36.
105. Bhutia YD, Ganapathy V. Glutamine transporters in mammalian cells and their functions in physiology and cancer. Biochim Biophys Acta 2016;1863:2531–9.
106. Wilder CS, Chen Z, DiGiovanni J. Pharmacologic approaches to amino acid depletion for cancer therapy. Mol Carcinog 2022;61:127–52.
107. Montero JC, Del Carmen S, Abad M, Sayagués JM, Barbáchano A, Fernández-Barral A, et al. An amino acid transporter subunit as an antibody-drug conjugate target in colorectal cancer. J Exp Clin Cancer Res 2023;42:200.
108. Encarnación-Rosado J, Sohn ASW, Biancur DE, Lin EY, Osorio-Vasquez V, Rodrick T, et al. Targeting pancreatic cancer metabolic dependencies through glutamine antagonism. Nat Cancer 2024;5:85–99.
109. Yokoyama Y, Estok TM, Wild R. Sirpiglenastat (DRP-104) induces antitumor efficacy through direct, broad antagonism of glutamine metabolism and stimulation of the innate and adaptive immune systems. Mol Cancer Ther 2022;21:1561–72.
110. Lee MS, Dennis C, Naqvi I, Dailey L, Lorzadeh A, Ye G, et al. Ornithine aminotransferase supports polyamine synthesis in pancreatic cancer. Nature 2023;616:339–47.
111. Parker SJ, Amendola CR, Hollinshead KER, Yu Q, Yamamoto K, Encarnación-Rosado J, et al. Selective alanine transporter utilization creates a targetable metabolic niche in pancreatic cancer. Cancer Discov 2020;10:1018–37.
112. Sharma P, Hu-Lieskovan S, Wargo JA, Ribas A. Primary, adaptive, and acquired resistance to cancer immunotherapy. Cell 2017;168:707–23.
113. Zhang J, Huang D, Saw PE, Song E. Turning cold tumors hot: from molecular mechanisms to clinical applications. Trends Immunol 2022;43:523–45.
114. Liu X, Song J, Zhang H, Liu X, Zuo F, Zhao Y, et al. Immune checkpoint HLA-E:CD94-NKG2A mediates evasion of circulating tumor cells from NK cell surveillance. Cancer Cell 2023;41:272–87.e9.
115. Berrien-Elliott MM, Jacobs MT, Fehniger TA. Allogeneic natural killer cell therapy. Blood 2023;141:856–68.
116. Kennedy PR, Felices M, Miller JS. Challenges to the broad application of allogeneic natural killer cell immunotherapy of cancer. Stem Cell Res Ther 2022;13:165.
117. Shiroishi M, Kuroki K, Tsumoto K, Yokota A, Sasaki T, Amano K, et al. Entropically driven MHC class I recognition by human inhibitory receptor leukocyte Ig-like receptor B1 (LILRB1/ILT2/CD85j). J Mol Biol 2006;355:237–48.
118. Leijonhufvud C, Reger R, Segerberg F, Theorell J, Schlums H, Bryceson YT, et al. LIR-1 educates expanded human NK cells and defines a unique antitumor NK cell subset with potent antibody-dependent cellular cytotoxicity. Clin Transl Immunol 2021;10:e1346.
119. Hallermalm K, Seki K, Wei C, Castelli C, Rivoltini L, Kiessling R, et al. Tumor necrosis factor-alpha induces coordinated changes in major histocompatibility class I presentation pathway, resulting in increased stability of class I complexes at the cell surface. Blood 2001;98:1108–15.
120. Alspach E, Lussier DM, Schreiber RD. Interferon γ and its important roles in promoting and inhibiting spontaneous and therapeutic cancer immunity. Cold Spring Harb Perspect Biol 2019;11:a028480.
121. Alimonti J, Zhang QJ, Gabathuler R, Reid G, Chen SS, Jefferies WA. TAP expression provides a general method for improving the recognition of malignant cells in vivo. Nat Biotechnol 2000;18:515–20.
122. Hanalioglu D, Ayvaz DC, Ozgur TT, van der Burg M, Sanal O, Tezcan I. A novel mutation in TAP1 gene leading to MHC class I deficiency: report of two cases and review of the literature. Clin Immunol 2017;178:74–8.
123. Jiang J, Taylor DK, Kim EJ, Boyd LF, Ahmad J, Mage MG, et al. Structural mechanism of tapasin-mediated MHC-I peptide loading in antigen presentation. Nat Commun 2022;13:5470.
124. Natarajan K, Dimasi N, Wang J, Margulies DH, Mariuzza RA. MHC class I recognition by Ly49 natural killer cell receptors. Mol Immunol 2002;38:1023–7.
125. Panda AK, Gangaplara A, Buszko M, Natarajan K, Boyd LF, Sharma S, et al. Cutting edge: inhibition of the interaction of NK inhibitory receptors with MHC class I augments antiviral and antitumor immunity. J Immunol 2020;205:567–72.
126. Verneris MR, Karimi M, Baker J, Jayaswal A, Negrin RS. Role of NKG2D signaling in the cytotoxicity of activated and expanded CD8+ T cells. Blood 2004;103:3065–72.
127. Qian L, Zhang Y, Pan XY, Ji MC, Gong WJ, Tian F. IL-15, in synergy with RAE-1ε, stimulates TCR-independent proliferation and activation of CD8(+) T cells. Oncol Lett 2012;3:472–6.
128. Lerner EC, Woroniecka KI, D'Anniballe VM, Wilkinson DS, Mohan AA, Lorrey SJ, et al. CD8(+) T cells maintain killing of MHC-I-negative tumor cells through the NKG2D-NKG2DL axis. Nat Cancer 2023;4:1258–72.
129. Wong JM, Malec PA, Mabrouk OS, Ro J, Dus M, Kennedy RT. Benzoyl chloride derivatization with liquid chromatography-mass spectrometry for targeted metabolomics of neurochemicals in biological samples. J Chromatogr A 2016;1446:78–90.
130. Hao Y, Hao S, Andersen-Nissen E, Mauck WM III, Zheng S, Butler A, et al. Integrated analysis of multimodal single-cell data. Cell 2021;184:3573–87.e29.